

Article

Towards Multiscale and Multisource Remote Sensing Mineral Exploration Using RPAS: A Case Study in the Lofdal Carbonatite-Hosted REE Deposit, Namibia

René Booyen ^{1,2,*}, Robert Zimmermann ¹, Sandra Lorenz ¹, Richard Gloaguen ¹, Paul A. M. Nex ², Louis Andreani ¹ and Robert Möckel ¹

¹ Helmholtz-Zentrum Dresden-Rossendorf, Helmholtz Institute Freiberg for Resource Technology, Division of Exploration, Chemnitz Str. 40, 09599 Freiberg, Germany; r.zimmermann@hzdr.de (R.Z.); s.lorenz@hzdr.de (S.L.); r.gloaguen@hzdr.de (R.G.); l.andreani@hzdr.de (L.A.); r.moekel@hzdr.de (R.M.)

² School of Geosciences, University of the Witwatersrand, 1 Jan Smuts Avenue, Braamfontein, 2000 Johannesburg, South Africa; paul.nex@wits.ac.za

* Correspondence: r.booyen@hzdr.de

Received: 2 September 2019; Accepted: 23 October 2019; Published: 25 October 2019



Abstract: Traditional exploration techniques usually rely on extensive field work supported by geophysical ground surveying. However, this approach can be limited by several factors such as field accessibility, financial cost, area size, climate, and public disapproval. We recommend the use of multiscale hyperspectral remote sensing to mitigate the disadvantages of traditional exploration techniques. The proposed workflow analyzes a possible target at different levels of spatial detail. This method is particularly beneficial in inaccessible and remote areas with little infrastructure, because it allows for a systematic, dense and generally noninvasive surveying. After a satellite regional reconnaissance, a target is characterized in more detail by plane-based hyperspectral mapping. Subsequently, Remotely Piloted Aircraft System (RPAS)-mounted hyperspectral sensors are deployed on selected regions of interest to provide a higher level of spatial detail. All hyperspectral data are corrected for radiometric and geometric distortions. End-member modeling and classification techniques are used for rapid and accurate lithological mapping. Validation is performed via field spectroscopy and portable XRF as well as laboratory geochemical and spectral analyses. The resulting spectral data products quickly provide relevant information on outcropping lithologies for the field teams. We show that the multiscale approach allows defining the promising areas that are further refined using RPAS-based hyperspectral imaging. We further argue that the addition of RPAS-based hyperspectral data can improve the detail of field mapping in mineral exploration, by bridging the resolution gap between airplane- and ground-based data. RPAS-based measurements can supplement and direct geological observation rapidly in the field and therefore allow better integration with in situ ground investigations. We demonstrate the efficiency of the proposed approach at the Lofdal Carbonatite Complex in Namibia, which has been previously subjected to rare earth elements exploration. The deposit is located in a remote environment and characterized by difficult terrain which limits ground surveys.

Keywords: mineral exploration; Remotely Piloted Aircraft System; hyperspectral sensors; multiscale; carbonatite complex; Namibia

1. Introduction

The increasing demand for raw materials worldwide conflicts, with the growing difficulties to find new mineral deposits, outlines the need for innovative approaches in mineral exploration. Technological advancements, such as green technologies and smart devices, have led in particular to an

increased demand for Rare Earth Elements (REEs). As a result, the exploration of new and promising REE deposits is of economic importance in view of the current dependence of the world market on imports from a limited number of countries.

Carbonatites, rocks comprising more than 50 modal-% carbonate minerals, are the main source of REEs [1]. The typical ore minerals for light rare earth elements (LREEs) are monazite, bastnaesite, and parisite, and for the heavy rare earth elements (HREEs), is xenotime [1]. Hyperspectral remote sensing has been recently suggested to detect and identify carbonatites as potential REE deposits [2–4], due to the distinctive absorption feature of carbonates (CO₃) around 2300 to 2350 nm [5]. At a sufficient grade, REEs can be detected directly due to their characteristic narrow absorption features in the VNIR and SWIR [3,6]. Neodymium (Nd) is a key element that can be used as a pathfinder for other REEs, on account of its particularly prominent absorption features at 580, 740, and 800 nm [3]. However, a very good signal-to-noise ratio and high spectral and spatial resolution are necessary to detect the characteristic absorption features of REE compounds [7]. So far, only close-range hyperspectral imaging (up to 10 m sensor-target distance) has allowed in situ detection of REEs [2].

For some time, remote sensing exploration has centered on the use of low-spatial-resolution, inexpensive satellite data, and costly airborne surveys. The overall mineral exploration scheme usually starts with mapping alteration zones and lithology using space and airborne remote sensing techniques. However, REE-bearing carbonatites usually occur as small structures, such as dykes and plugs, thus a sufficient spatial resolution is imperative for their identification. Satellite sensors can image large areas, but freely available data have limited spatial resolutions, typically 10–30 m. The spectral bands of multispectral satellite-based sensors, such as ASTER, are broad and noncontiguous. Even the carbonate features cannot be accurately detected by the low spectral and spatial resolutions of ASTER, unless the exposures are relatively large and thickly bedded [8]. Hyperion, the only hyperspectral civil satellite with global coverage currently available, has a poor signal-to-noise ratio, other artifacts in the data and has limited coverage [9,10]. Additionally, the spatial resolution of Hyperion archived data is not adequate in detecting the small REE features. Even other planned satellite missions, such as EnMAP, HypIRI, HISUI, and PRISM, with improved SNR, have a too coarse spatial resolution of between 20 and 30 m, and will not solve this problem.

Aircraft-based systems usually achieve finer spatial resolutions, but only cover intermediate areas and are costly to deploy. Plane-based hyperspectral data publicly available in Namibia (HyMap) have relatively coarse spectral bands (~15 nm) [11]. REE absorptions features are typically very narrow and thus cannot be detected by these data. In addition, the available HyMap data features a spatial sampling distance of 4.5 m, which does not allow detection of very small geological structures, such as the typical dykes, or lenses known to host REE deposits. A preliminary study demonstrated these difficulties to successfully delineate rather small dykes enriched in REEs using airborne sensors [12]. One way to tackle this problem is through the integration of different sensors at different resolution levels. Recent work aims at improving the identification of targets for mineral exploration by combining information from multisensor sources as well as geomorphological data in the spectral mapping scheme [13,14].

A way to mitigate the problem is potentially provided by the development of Remotely Piloted Airborne Systems (RPAS). Imaging spectroscopy (IS) using RPAS represents a novel, still developing field in modern remote sensing technologies. Compared to airborne remote sensing, RPAS offer cost-effective image data collection at significantly finer spatial resolution, but smaller spatial coverage. An important advantage of the RPAS-based technologies is that optical image data can be collected even under nonoptimal weather conditions such as partial or full cloud cover [15]. This difference makes RPAS-based technologies potentially truly operational for a wide range of environmental applications, especially those focusing on diverse dynamic phenomena.

The first lightweight optical RPAS systems used commercial video cameras or cameras operating in three broad-bandwidths (RGB) and/or near-infrared spectral regions [16]. Contrary to those broad-band visible-spectrum cameras, which have reached weights of hundreds of grams and resolution of tens of megapixels, the miniaturization of multi- and hyperspectral cameras is still challenging in terms of optics

and sensor calibration [17]. However, there have recently been some multi- and hyperspectral cameras made available for the scientific community [17–19]. These multi- and hyperspectral lightweight sensors cover the visible to near-infrared (VNIR) spectral range (400–1000 nm) with tens of narrow bands and provide images with high radiometric quality [18–20]. So far, these cutting edge technologies and methods have been used primarily for analyzing vegetation, such as crop monitoring [19,21], forest fire monitoring [22], vegetation indices [23], and analysis of Antarctic moss bends [18]. Aside vegetation, the VNIR spectral range can bring valuable information on other objects of the interest such as Fe³⁺-bearing minerals [20], alteration minerals [24], rare earths [6], organic component [25] and optically active water substances [26]. Because of a relatively unstable platform and extremely challenging acquisition geometries with respect to sun illumination, very minute corrections are required [27,28].

We propose an integrated remote sensing approach utilizing all the different levels of data resolutions to address these challenges; from satellite- to aircraft- to RPAS-based. The multiscale and multisource data combination entails the full scope of available remote sensing imaging solutions from space-borne to RPAS-based sensors as well as a dedicated field campaign for training and validation of the algorithms. We propose to use the advantages of each sensor in an integrated way. We first identify large structures that potentially encompass areas of interests using satellite-based data. We then focus on promising sites utilizing the higher spatial and spectral resolutions of plane-based data. Small and very local geological structures are then mapped at high spatial resolution with RPAS-based sensors. Through the use of RPAS-based exploration, an extremely high spectral and spatial resolution can be achieved for the detection and characterization of small-scale structures. Geomorphometric analyses provide additional contextual information to improve classification accuracies by integrating spectral and topographical contents. Ground sampling campaigns (field observations and radiometric data) are used for cross-validation and accuracy assessments of the mineral maps.

The demonstration site, Lofdal Farm, is situated in Northern Namibia, where several REE hosting structures have been identified and are currently explored [29,30]. Its location in a semi-arid area and the existence of sufficient in situ data for validation were key in that selection. The Lofdal area comprises a swarm of small-scale carbonatite dykes. The genesis of the REE mineralization is still debated however, a late hydrothermal origin of the ore bearing fluids is generally proposed [31]. As the enrichment of REE minerals in any hydrothermal system is strongly concentrated along localized weakness zones, a precise structural mapping is required. This study area provides unique conditions to demonstrate the benefits of RPAS surveys for the remote sensing mapping of fine geological structures and to evaluate the synergic potential of multisensor techniques.

2. Geological Setting: Demonstration on the Lofdal Deposit

The Lofdal area was chosen as demonstrator, but is only one of the localities identified on remote sensing data. We focus on Lofdal because it is the area which has been studied most.

The Lofdal Alkaline Carbonatite Complex, aged ~750 Ma [32], is located on the Bergville and Lofdal farms, 35 km NW from Khorixas in the Kunene region of Namibia. The Paleo-Proterozoic Huab Basement Complex hosts the alkaline complex and is made up of metasedimentary gneiss and schist. The geometry is composed of a plug-like syenite–carbonatite intrusion known as the Main intrusion with a smaller plug-like body, called the Emanyia intrusion, 5 km to the SW. The complex contains a swarm of roughly E–W striking carbonatite dykes as well as smaller plugs of calcite carbonatite [32] (Figure 1). These carbonatite plugs and dykes combined with the occurrence of phonolite, syenite, and mafic dykes, and plugs form together the alkaline intrusive complex [33]. Jung et al. [34] has proposed a two-stage model of emplacement based on isotopic compositions to explain the syenite–carbonatite suite intrusion. The first stage is partial melting of the upper-mantle followed by the second stage of differentiation of unexposed alkali-basaltic magma.

The Lofdal Alkaline Carbonatite Complex is unique in its unusually high enrichment of HREEs compared to the LREEs [35]. Xenotime-(Y) is the principal HREE host mineral and generally occurs in

the iron-rich calcite carbonatite dykes. The xenotime is associated with iron oxides, thorite, apatite and synchysite-(Ce) [35]. Although the genesis of REE mineralization at Lofdal is still debated, it has been suggested lately that HREE enrichment is likely related to hydrothermal processes [36].

Several areas with high potential for REE explorations have been identified by the exploration team in the past. Such an area, known as Area 4, which lies ~1 km SE from the main intrusion, has received much attention, and has been studied extensively over the years [29,30]. However, for this study we focus on Area 1, a relatively understudied area compared with Area 4, but very typical of the entire site in terms of mineralogy. Area 1 is located North-East of the main intrusion and consists of dozens of carbonatite dykes, some of which cross-cut each other (Figure 1). The dykes are tens of meters long and are 0.5 cm to 1 m wide. This characteristic geological setting is used to evaluate the benefits of RPAS for the geological mapping of complex and small-scaled structures.

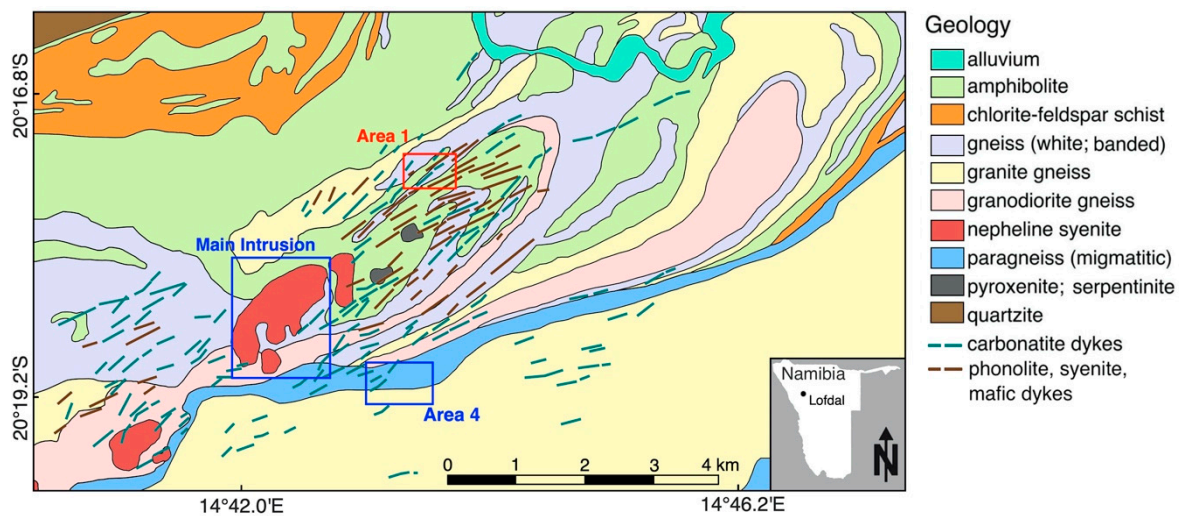


Figure 1. Geological map of the Lofdal Alkaline Carbonatite Complex, including the location of the dyke swarms. Area 1 is located northeast from the Main intrusion (adapted from the Geological Survey of Namibia).

3. Methodology and materials

3.1. General Workflow

The proposed approach uses data captured from platforms with decreasing altitudes (Figure 2) and envisages a holistic workflow taking into account local characteristics, such as vegetation cover and geology, as well as data availability. This is especially beneficial as the resolution of the data being captured increases systematically (Figure 3). Dedicated analyses were performed on the data at varying resolution levels and are summarized in Figure 4. Each analysis is explained in detail in section “Processing and field validation”.

In the first step, we applied commonly used spectral analyses, known for their versatility and robustness, on satellite- and aircraft-based imagery. We chose ASTER data for the first level of resolution and performed lithological mapping and area identification (top section of Figure 4). We mapped the main lithologies of the region by performing selected band ratios. The next level of resolution is provided by plane-based imaging. We performed band ratios and minimum wavelength mapping (MWM) on HyMap imagery and used the results to refine an area of interest (Top section of Figure 4). Once we chose and refined the area of interest, we moved to the next resolution level using RPAS-based sensors. RPAS-based sensors can capture the spectral and topographical data needed to study small scale features (middle and bottom sections of Figure 4).

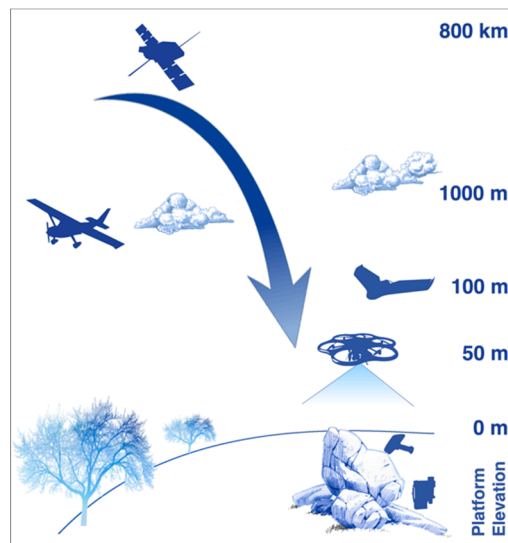


Figure 2. The approach taken to improve mineral exploration. Entailing the use of remote sensing platforms; from satellite-, to airborne-, to Remotely Piloted Aircraft System (RPAS)-based data acquisition, as well as field validation with remote sensing and geochemical measurements.

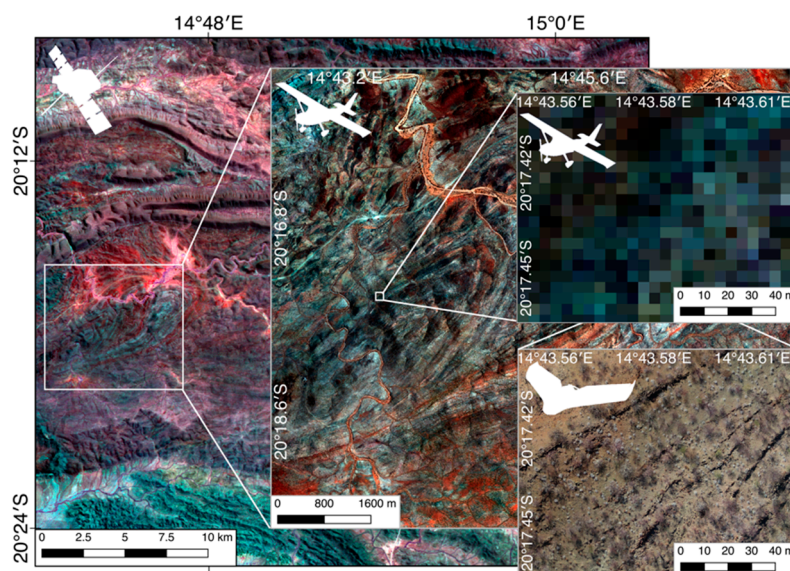


Figure 3. Visual representation of the increase in spatial resolution from satellite sensors, to aircraft- to the high spatial resolution of RPAS-based sensors.

Field scouting backed by literature show that the REE occurrences are hosted in carbonatite dykes in the study area [33]. Field observation showed that these structures are topographically elevated in a relatively flat surrounding terrain. Therefore, the best field approach was to capture RPAS-based data over the area and to use both spectral and topographic information in parallel. Structure-from-motion multi-vision-stereo (SfM-MVS) photogrammetry was performed on the orthophotos obtained by a fixed-winged RPAS and a Digital Elevation Model (DEM) was created. The photogrammetry procedure is explained further in Appendix A. Subsequently, the DEM was used to automatically map the dykes (Middle section of Figure 4). The structural and textural analyses were performed using TecGEMS, a Python-based toolbox, which is being developed by Andreani L., Pohl E. and Gloaguen R. [37].

The final level of resolution consists of hyperspectral RPAS-based imagery which was captured with a hexacopter (Bottom section of Figure 4). The RPAS-based hyperspectral data requires specific preprocessing steps and is performed with an in-house toolbox called MEPHySTo (See Appendix A) [28]. After the preprocessing of the RPAS-based hyperspectral imagery, we performed a combination of

spectral analyses on the data to map potential REE zones. Spectral Angle Mapper (SAM), Spectral Information Divergence (SID), and MWM were used and compared with one another. MWM is usually preferred as it is fitted to a specific spectral signature. On the other hand, due to the low concentration of target minerals and limited spatial resolutions and SNR of existing sensors, absorption features might be difficult to identify. In that case, classification methods, such as SID and SAM, can provide an indirect tool to identify either the target minerals or proxies. Field work was then performed in the refined study area and included traditional field exploration techniques, such as field mapping and representative sampling.

The workflow developed here is versatile as it can easily be adapted to a wide range of commodities and makes use of commonly available datasets and procedures. The use of airborne data is not required but provides valuable information if the data are available. The parameters used in the workflow can easily be tuned by a geologist with some knowledge of remote sensing techniques to adapt the procedure to the geological conditions and the type of ore deposit targeted.

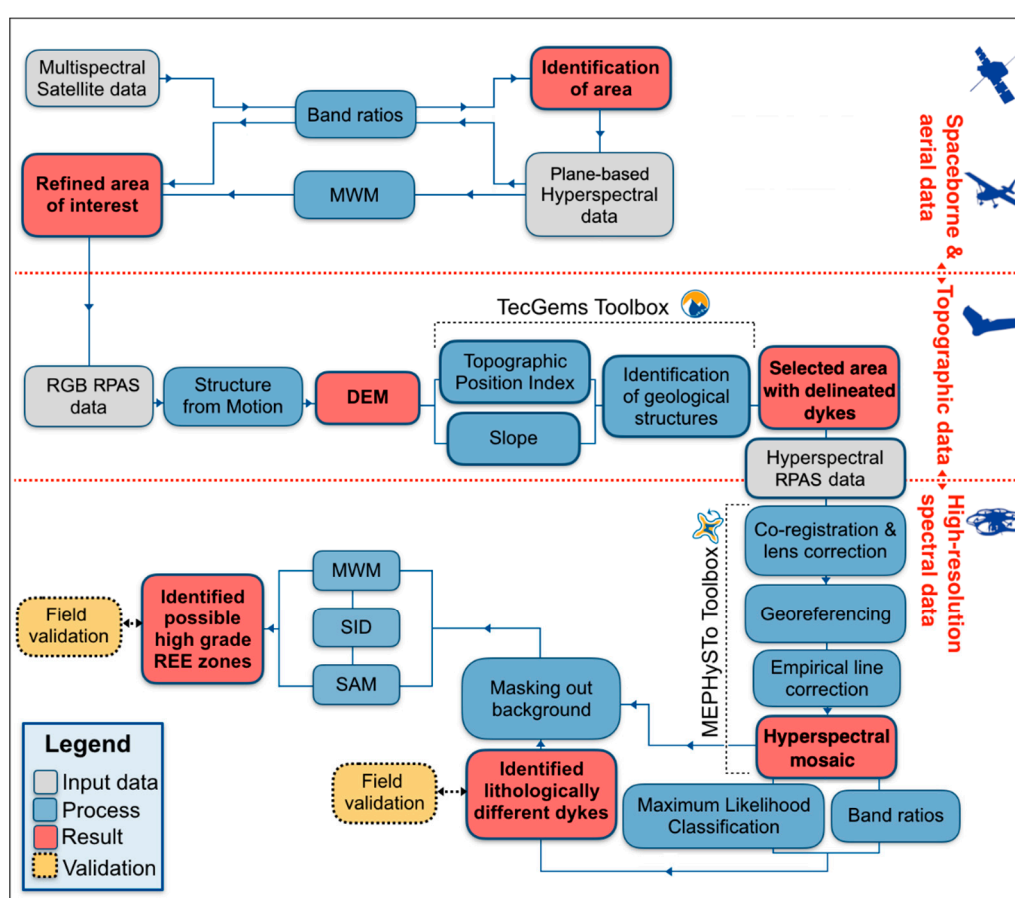


Figure 4. The processing workflow of the data captured at Lofdal. The data captured consisted of satellite, airplane-, and RPAS-based. It indicates the integration of topographic with spectral information. The top section of the workflow depicts the processing methods performed on the ASTER and HyMap data while the middle and lower sections show the processing methods performed on the RPAS-based data.

3.2. Data Acquisition and Preprocessing

Preprocessing of the data, which entails image corrections of multi- and hyperspectral data sets, is a paramount step for the accurate analyses of spectral information, and is performed before further analysis such as spectral classifications. Although they are based on the same principles, the preprocessing steps will differ for each platform according to specific requirements; satellite sensors

will require atmospheric corrections unlike RPAS-borne sensors which will need corrections such as lens distortions and band co-registration. The satellite, plane-, and RPAS-based data sets we used have increasing spectral and spatial resolutions and their spectral ranges are visualized in Figure 5. A list of all the platforms and sensors used in the workflow is summarized in Table 1 and the spatial footprints of each data set can be found in Figure 6. Three areas (known as Area 1, Area 4, and Area 5) were surveyed with RPAS, and Area 1 was chosen as demonstration in this article due to its representative geology in the complex and its potential of high HREEs concentration.

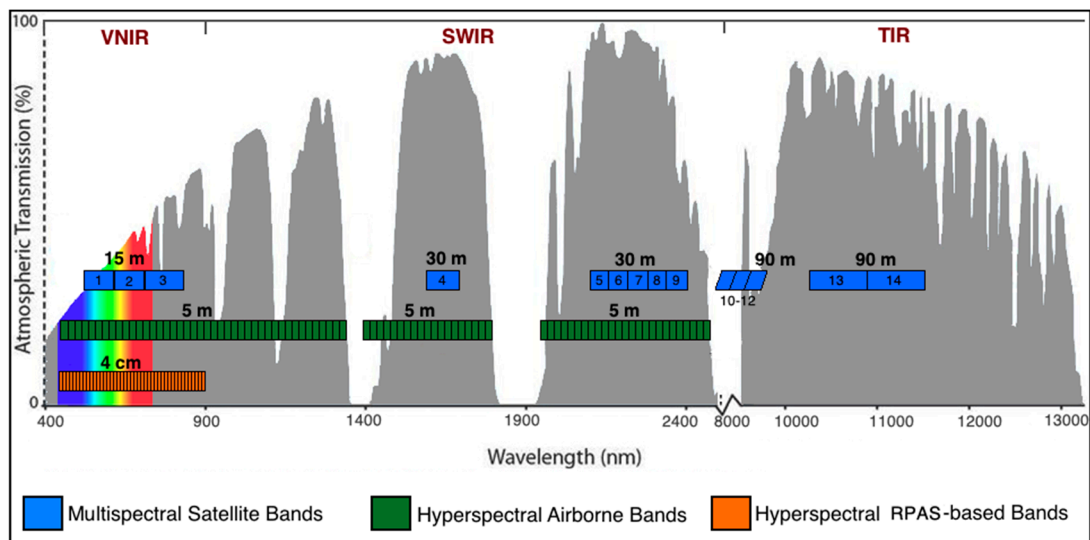


Figure 5. Diagram showing the spectral information of each data set; spectral size and range of multispectral satellite (ASTER) bands, hyperspectral airborne (HyMap) bands, and hyperspectral RPAS-based bands. The spatial resolution of the various data sets is indicated above each set of bands.

Table 1. Summary of platforms and sensors utilized in this study; the parameters and general use are listed next to each sensor.

Spectral Sensors					
Platforms	Sensor	Parameters	SNR	Spatial Resolution	Purpose
Satellite-based	ASTER: Multispectral pushbroom sensor	B1 (520–600 nm) B2 (630–690 nm) B3 (760–860 nm) B4 (1600–1700 nm) B5 (2145–2185 nm) B6 (2185–2225 nm) B7 (2235–2285 nm) B8 (2295–2365 nm) B9 (2360–2430 nm)	B1–B4: 140 @ 70% albedo B5–B7 & B9: 54 @ 70% albedo B8: 70 @ 70% albedo	VNIR (B1–B3): 15 m SWIR (B4–B9): 30 m	Spaceborne multispectral imaging
Plane-based	HyMap: Hyperspectral whiskbroom sensors	126 spectral channels Band width 15–20 nm Spectral range from 450–2500 nm	All channels: 1000:1 [11]	4.5 m	Aerial hyperspectral imaging
RPAS-based: Aibotix Aibot x6v2 (hexacopter)	Rikola hyperspectral Imager	50 spectral channels (in aerial mode) Band width at ~10 nm Spectral range from 500 nm–900 nm	All channels: 150:1 [38]	6.5 cm at 100 m	High resolution aerial hyperspectral imaging
RPAS-based: SenseFly eBee (Fixed-wing)	Canon Powershot S110 RGB camera	Nadir stereo-photos.	n/a	4.9 cm at 120 m	Photogram-metry

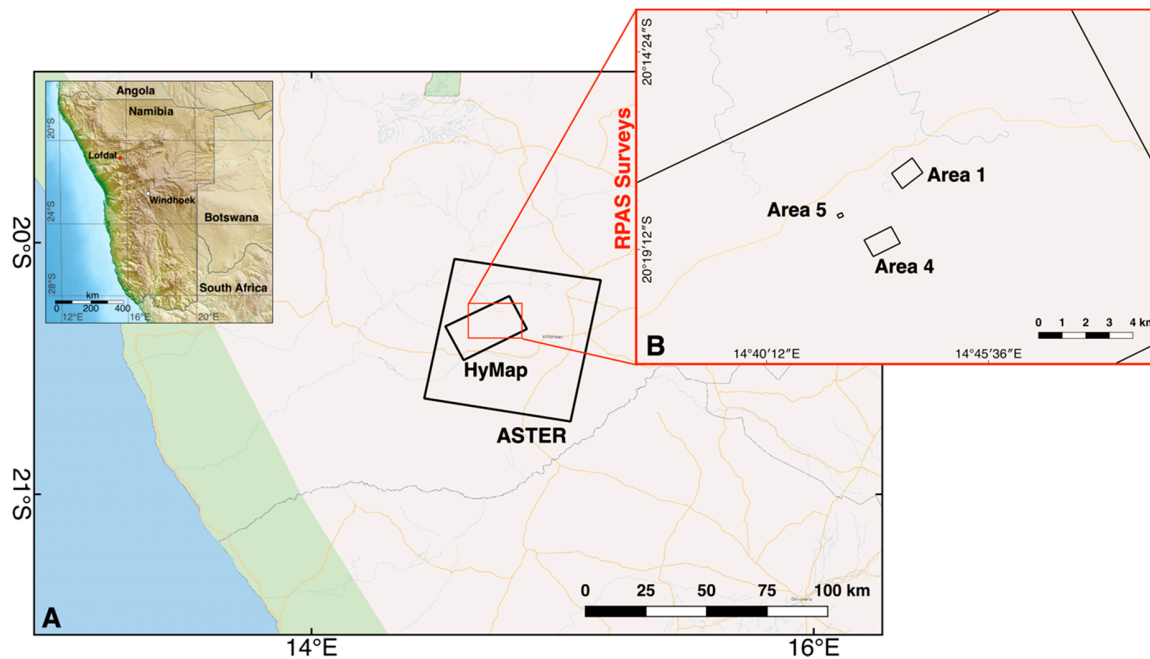


Figure 6. Geographic map showing the spatial extent covered by each data set including an inset of a topographic map of Namibia depicting the location of the Lofdal area. (A) Spatial footprints of ASTER and HyMap data. (B) Spatial foot prints of the areas covered with RPAS-based surveys.

3.2.1. Satellite and Plane-based Sensors

We favor open source satellite data to ensure availability and decrease costs. ASTER data was specifically chosen for this project because of its higher amount of SWIR bands compared to other multispectral satellite sensors such as Landsat. However, Sentinels, SPOT and Landsat data could also be considered. Geological spectral features are mostly situated in the SWIR region of the electromagnetic spectrum and thus other studies have proven the effectiveness of lithological mapping using ASTER imagery [39,40]. The ASTER scene over the study area in Namibia was acquired on 21/09/2006. The sensor parameters are listed in Table 1. The ASTER data was atmospherically corrected using the Fast Line-of-sight Atmospheric Analysis of Spectral Hypercubes (FLAASH) tool in ENVI. The FLAASH atmospheric correction tool can be applied to VNIR and SWIR data and is based on the MODTRAN model [41]. Due to the varying resolutions of the spectral channels of the ASTER data, the VNIR bands were resampled from 15 m resolution to 30 m to match the SWIR band resolution before further analyses.

HyMap is an aircraft-mounted hyperspectral sensor operated by the HyVista corporation and developed by Integrated Spectronics [42]. The sensors parameters are summarized in Table 1. Available aerial hyperspectral data over Lofdal were processed in order to map relatively small scale geological features. The HyMap data provided by HyVista were already fully corrected and ready-to-use with a spatial resolution of 4.5 m. The preprocessing done by the HyVista team consists of radiance and atmospheric calibration as well as geometric corrections [42].

3.2.2. RPAS-based Sensors

Surveys were performed with two types of RPAS, a fixed-wing system and a multicopter (cf. Table 2). Selected areas are mapped using hyperspectral imaging (HSI) and SfM-MVS photogrammetry. The two sensors require specific flight characteristics and acquisition procedures [28]. The frame-based hyperspectral camera needs a stable platform at the time of image acquisition to allow a sufficient integration time and low spatial shift between single bands. The fixed-wing RPAS (Sensefly eBee) has a longer flight time than the multicopter, and can thus cover a larger area size and acquires nadir

stereo-photos as input for SfM-MVS photogrammetry. The eBee has a maximum flight time of 50 min and is equipped with a Canon Powershot S110 digital camera with a resolution of 16MP (Table 2). A predefined flight-route with GPS waypoint is created and uploaded onto the RPAS before take-off. The flight line spacing is determined in such a way that there is a high overlap of the aerial photographs (85% forward lap and 70% side lap).

Table 2. RPAS and flight parameters over Area 1, Lofdal.

Information	Photogrammetry	Hyperspectral Imaging
RPAS	Sensefly eBee	Aibotix Aibot X6v2
Camera system	Canon S110 RGB camera	Rikola Hyperspectral Imager
Flight altitude (Above take-off)	120 m	50 m
Flight time	35 min, 27 s	9 min, 44 s
Sensor resolution	4608 × 3456 px (15.9 MP)	1011 × 648 px (0.65 MP)
Ground sampling distance (GSD)	4.9 cm/px	3.25 cm/px
Number of Images	215	32
Area covered	0.961 km ²	0.0038 km ²

3.3. Processing and Field Validation

3.3.1. Satellite and Airborne Approach

Even though it is not possible to directly detect small carbonatite bodies with ASTER imagery due to its low spatial resolution, we used indicators in the regional geology to locate ideal areas where they might occur. Normally, carbonatites occur as small bodies within alkalic intrusive complexes, and the emplacement of carbonatite intrusions are commonly accompanied by hydrothermal alteration of the country rock [43,44]. The hydrothermal fluids can introduce REEs into the system. Thus, we have summarized two main indicators to locate possible occurrences of REE-bearing carbonatites. (1) We identify alkali rocks which can be associated with carbonatites. (2) We locate regions of deformation which could have facilitated hydrothermal activity (Figure 7A).

With these two indicators in mind, a smaller area of interest was chosen and analyzed using HyMap data (Figure 7B). However, we were not able to detect REE-rich regions with the HyMap data. To map REEs, their concentrations within a pixel must be such that absorption features will occur in the spectra. This is only possible if the pixel size matches the areas of high concentration. REEs are usually found in small concentrations zones within larger rock formations. A higher ground resolution than what HyMap (resolution of 4.5 m) can offer is thus required. Thus, we decided on a different indicator for possible REE-rich areas. A link between the presence of iron and REEs has been suggested by Salminen et al., (2005). With the HyMap data, we were able to select promising regions containing both these carbonatite and iron features. We selected three promising regions to demonstrate our field work approach involving RPAS (Figure 7C,D). One area was specifically chosen because the exploration company who owns the exploration rights to Lofdal (Namibian Rare Earths) gave us access to the area (defined by Namibian Rare Earths as Area 1) and provided geochemical analyses of rock samples to validate our procedure.

RPAS-based data was then used to map the numerous dykes over a given area (Figure 7C) and characterized with RPAS-based hyperspectral data (Figure 7D). Field measurements with the handheld XRF and spectrometer indicated that there were primarily two sets of dykes, one set enriched with iron, and the other set contained very little iron. This allowed us to spectrally differentiate between the dykes based on chemical composition. Harmer and Nex [45] have noted that the highest REE concentrations are usually found in iron-rich carbonatites. Therefore, we decided to focus on the iron-rich dyke to test whether we can map REE-rich zones using RPAS-based sensors.

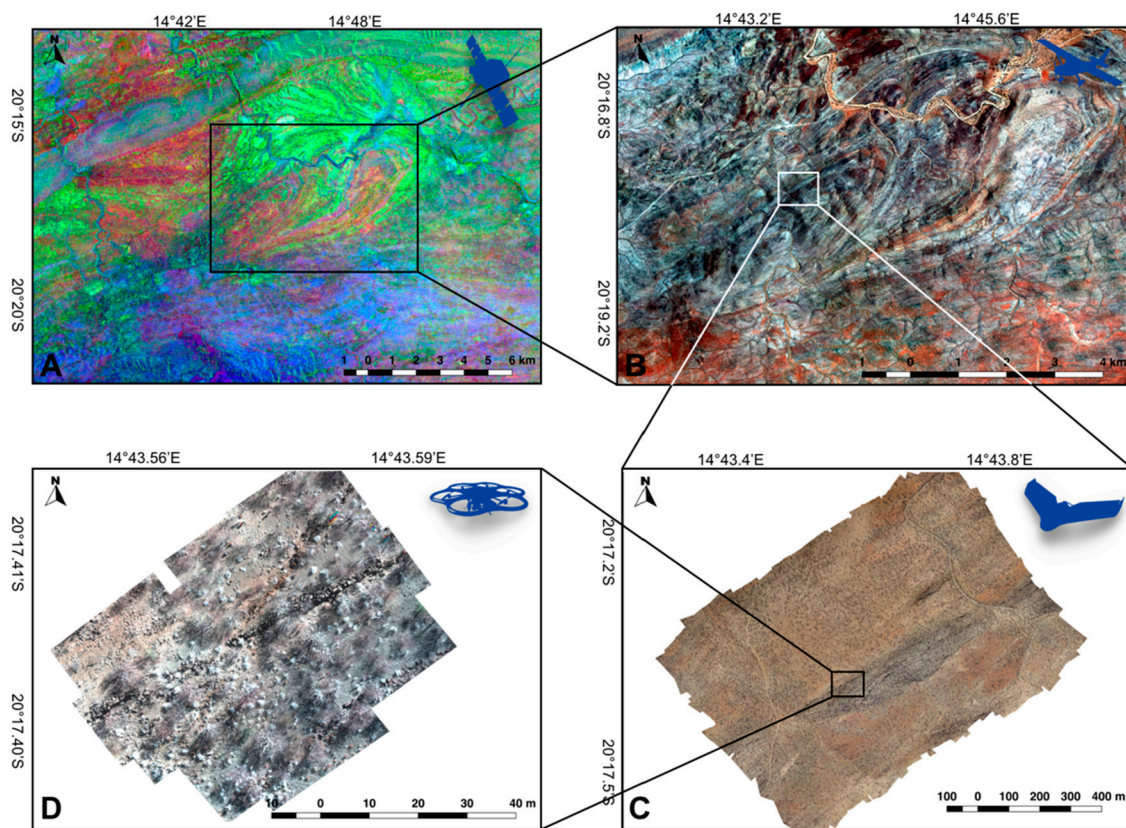


Figure 7. Diagram showing the various platforms used for multi- and hyperspectral imaging and the areas focused on with each platform. (A) False color composite of ASTER data showing lithological discrimination of the Lofdal area (B4/B7 - B4/B3 - B2/B1). (B) Near-infrared (NIR), green, and blue HyMap image of Lofdal. (C) Orthophoto of Lofdal. (D) High-resolution RGB image from the Rikola showing individual dykes.

3.3.2. Spectral Analyses

Band ratios were specifically chosen for their proven robustness and applied to the ASTER imagery [46]. A combination of SWIR and VNIR bands enhances geological units, making lithological discrimination possible [47]. The band ratios chosen for this purpose were taken from Abrahams and Hook [47] and are as follows; B4/B7, B4/B3, and B2/B1 in the R-G-B channels, respectively. Band 7 is used to distinguish magnesium hydroxide and amphiboles while iron can be detected with the VNIR bands [48].

We performed band ratios and minimum wavelength mapping (MWM) in parallel on the HyMap data of a given area to investigate the geological features. Numerous studies have established the potential of band ratios to map iron occurrences, a general feature to distinguish lithologies [49,50]. Thus, an iron band ratio (769 nm/458 nm) was performed on the HyMap data. MWM is a procedure whereby the wavelength position of the deepest absorption features is mapped, and has been successfully used to distinguish minerals with strong spectral features [51]. This works best with hyperspectral data because of the high spectral resolution and contiguity of the bands allowing it to display narrow absorption features. This powerful method was used to map the distinct carbonate absorption feature at 2340 nm [52].

RPAS-based hyperspectral data was used to characterize dykes in a chosen area. We again used an iron band ratio to map and distinguish dykes in the image; the 760 nm wavelength was divided by the 880 nm wavelength to enhance the iron feature. We then mapped zones of REE occurrences within individual dykes using the same hyperspectral data. Pixels outside the analyzed dykes were masked. Both (1) direct and (2) indirect methods were used to identify zones possibly containing REEs within a dyke.

(1) Based on the results of laboratory tests, MWM was used to map the 800 nm absorption feature of Nd. Spectra measured by the Rikola imager in the laboratory has an approximate 7 nm shift to higher wavelengths (See Appendix B). Considering this spectral shift, a range was set between wavelengths 795 nm and 820 nm to map the deepest absorption feature within that region. Although it is the most direct way to map REE absorption features, noise in the spectra made it challenging to confidently detect minute absorption features.

(2) The spectral matching methods SAM and SID are supervised classification methods. SAM is a widely deterministic classification method in hyperspectral remote sensing and many studies have shown its effectiveness in mineral mapping [53,54]. Although SID is not as widely used, it also determines the similarity between a pair of spectra. SID, however, is a stochastic approach that can characterize spectral similarities more effectively than SAM [55]. We used the spectrometer to measure spectra along the dykes and created a library from spectra containing REE absorption features at 580 nm, 740 nm, and 800 nm. Of the in situ spectra collected, two measurement points showed positive REE absorption features. These spectra were averaged and used as the reference spectra for both SAM and SID methods. The idea is to find sections which are spectrally similar to host rocks containing REEs.

3.3.3. Extraction of structural features

The high-resolution DEM (Figure 8) obtained from SfM-MVS photogrammetry allows us to map linear features such as carbonatite dykes, which form narrow and shallow topographic ridges as a result of differential erosion. For this purpose, we propose to use a ridge detection algorithm. The algorithm locates the points of maximum curvature in the DEM which correspond to the surface trace of dykes. One common approach to analyze the curvature of elevation data is to use an eigenvalue analysis of the Hessian matrix [56,57]. The Hessian matrix is a 2×2 matrix composed of second-order partial derivatives of the input image, whereas the second-order partial derivatives are defined as a convolution with derivatives of Gaussian filter at scale σ . The idea behind eigenvalue analysis of the Hessian matrix is to extract the principal directions and magnitude in which the local second order structure of the image can be decomposed. Each pixel is associated to a set of eigenvectors $|\lambda_1|$ or $|\lambda_2|$. Linear features are characterized by a very small magnitude of λ_1 (ideally close to zero) and a large magnitude of λ_2 , whereas point features will be characterized by similar magnitudes of λ_1 and λ_2 and features without preferential directions will have low magnitudes for both λ_1 and λ_2 .

To apply this technique, we applied a low pass-filter to remove small artifacts such as boulders as well as accelerate the processing. The eigenvalue analysis was then performed on the resampled DEM using an initial Gaussian filter. Once the absolute magnitude of eigenvectors is extracted, a threshold is used in order to remove weak ridges (i.e., associated to a low curvature). This threshold was set to 75% of the maximum magnitude based on previous studies and experimentation. Ridges were then identified using a local maxima function (i.e., pixels higher than their neighbors along the x or y axis were tagged as "ridges"). Finally, identified ridges were vectorized by connecting neighboring tagged pixels. The final step is a simplification of extracted linear features. Segments smaller than 20 pixels (ca. 4 m) were discarded and the trace of remaining segments is simplified using the approach of Visvalingam and Whyatt [58]. One drawback of this approach is that other curvilinear features such as the edges of gullies may be falsely detected as well. For this reason, a manual cleaning is crucial and was performed in order to discard irrelevant features in a last step.

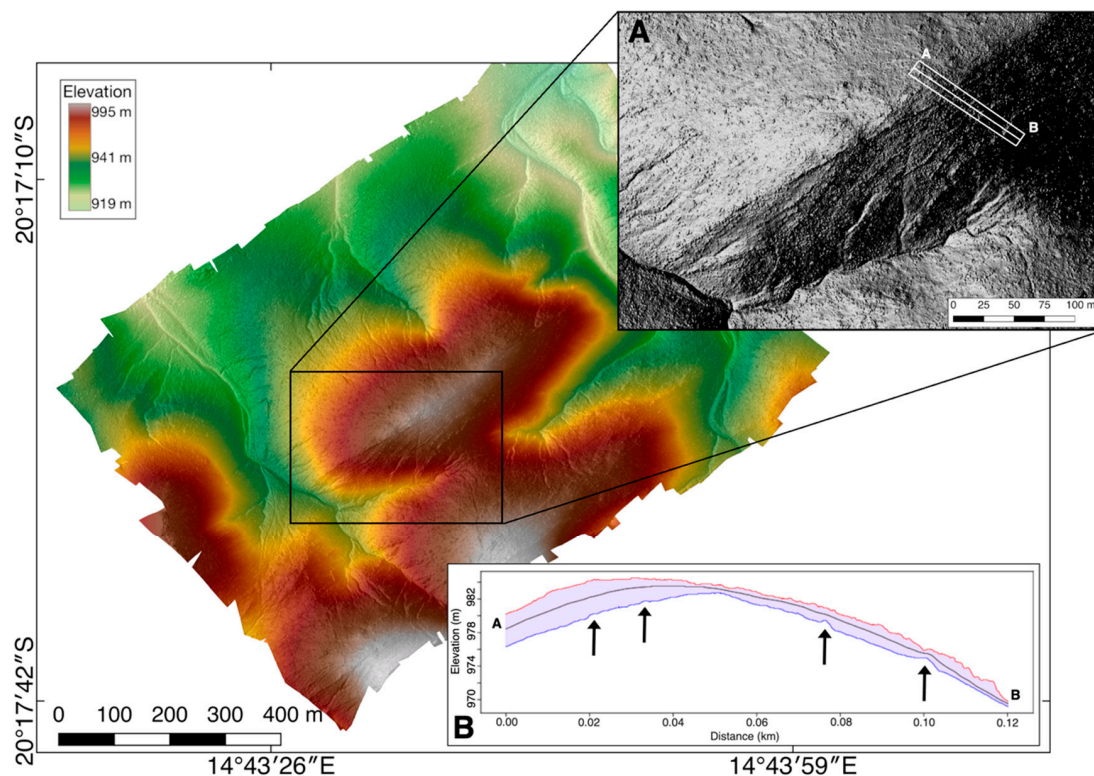


Figure 8. High-resolution Digital Elevation Model (DEM) of Area 1 (cf. Figure 6) derived from Structure-from-motion Multi-Vision-Stereo (SfM-MVS) photogrammetry with a ground resolution of 4.9 cm. Inset **A** shows a shaded relief section of the DEM where very fine geological structures can be discerned. Inset **B** shows a swath profile from points A to B, the black arrows point to possible dykes.

3.3.4. Validation and field procedure

Validation points were measured with a handheld XRF and a portable spectroradiometer, while their positions were recorded by a handheld GPS. Strike and dip of the outcropping carbonatite dykes in the study area were also measured. Both methods rapidly provide information about rock chemistry during field work and allow a better field planning.

A Spectral Evolution PSR-3500 portable spectroradiometer was used to measure the spectra of rock surfaces and hand samples. Spectra are recorded in the VNIR/SWIR region of the electromagnetic spectrum (400–2500 nm) using a contact probe (8 mm spot size) with artificial illumination. The spectral resolution in the VNIR range is 3.5 nm while the spectral resolution is 7 nm in the SWIR range. A precalibrated PTFE panel (Zenith polymer; >99% reflectance in the VNIR range and >95% in the SWIR) was used to convert the radiance values to reflectance. Each spectral record consists of 10 individual measurements taken consecutively and averaged.

A Bruker S1 Titan 800 handheld X-ray fluorescence spectrometer was used both in the field and laboratory, operated in Bruker's GeoChem calibration mode. The Bruker features a Rh target X-ray tube with a maximum acceleration voltage of 50kV at a maximum current of 0.2 mA and a Silicon Drift Detector (SDD). The X-ray emission in GeoChem mode is recorded between 0 to 45 kV in two separate phases: the 1st phase includes heavy elements ($\geq\text{Fe}$) and is recorded using a TiAl filter and 45 kV acceleration voltage, and the 2nd phase includes the light elements ($\leq\text{Fe}$) without a filter and 15 kV. The handheld XRF measured in situ geochemical information of the rock outcrops, giving us an estimate of iron and, via indicators (i.e., Y or Zr), the REE contents. The rapidly captured geochemical data roughly indicate REE mineralized areas, which aids us in determining focus areas. Consecutive XRF and XRD analysis of rock samples were measured in the laboratory to verify the field measurements as well as to validate spectral field information. Selected samples were sent for whole rock geochemical assay using ICP-MS fusion for major and selected trace elements.

4. Results from Lofdal

We performed dedicated band ratios on the ASTER data as mentioned in the section “Spectral analyses”, to identify areas which may contain carbonatite-hosted REEs and define a region of interest. The result enabled us to discriminate between the main lithologies of amphiboles, syenites, and gneisses, and possible alteration zones were highlighted by identifying iron (Figure 9A). The structure of the region was also discerned from the band ratio result, which were not entirely evident in the plain RGB image. We were able to map major faults by locating areas with offsets in the lithological layering (Figure 9A.1). We also detected highly curved structures indicating intense folding in the region (Figure 9A.2). The faulting and folding show that the area has undergone regional ductile deformation.

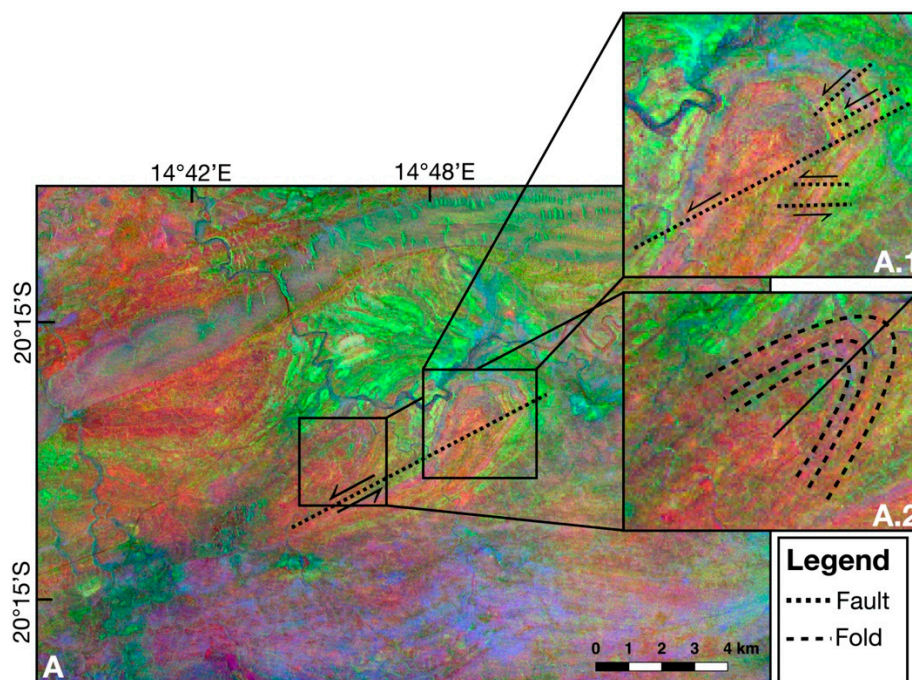


Figure 9. (A) False color composite of the band ratio results on ASTER data showing lithological discrimination (B4/B7, B4/B3, and B2/B1). (A.1) Major faults depicted. (A.2) Indication of folding.

We selected an area of interest close to alkali rock (the syenite intrusion) showing regional deformation, as a promising site for the occurrence of carbonatites. This area was investigated in more detail with HyMap data. The results of the iron band ratio and the regions rich in carbonates identified using MWM were overlain and the product can be seen in Figure 10. One of the selected areas containing both iron and carbonatites was used to demonstrate our RPAS-based field surveying.

The selected area contains numerous thin dykes. To map the dykes in this area, a better resolution than what satellite or plane-based data can offer is needed. The photogrammetric DEM derived from the eBee over a specific area of interest has a ground resolution of 4.9 cm and covers of approximately 1 km². Field validation supported by the DEMs to locate structures of interest confirmed that the dykes are mostly composed of carbonatites. Geological maps and available information provided by local geologists indicated that the dykes have not been thoroughly mapped in this area.

The dykes are not easily discernible from the DEM alone, and performing solely a manual extraction would be arduous and subjective. We, therefore, automatically mapped the dykes using morphological feature extraction (Figure 11A–D). The specific techniques and parameters are outlined in Table 3. A ridge detection algorithm was performed on elevation data (Figure 11A,B) and lineaments were automatically extracted (Figure 11C). Automatically extracted features were refined manually to map dykes in Area 1. We were able to map the dykes rapidly and remotely using this procedure. Approximately 45 dykes were mapped in the area. Overall, the dykes show a North-easterly trend.

A small area containing a complex pattern of dykes was selected for precise hyperspectral imaging with the multicopter mounted Rikola (Figure 11D).

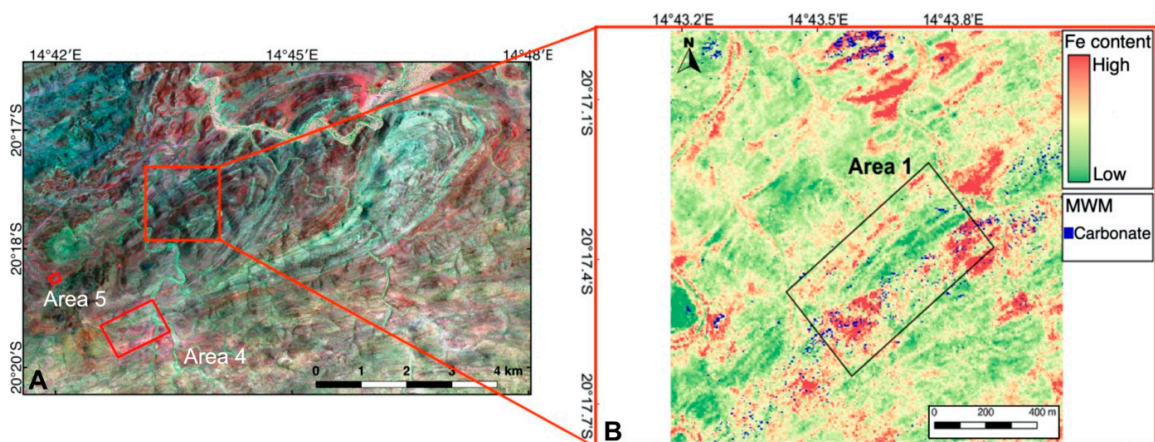


Figure 10. (A) False color composite HyMap image indicating the areas which have been surveyed with RPAS in red. (B) Band ratio performed on the main area of interest (764 nm/458 nm) enhancing the iron absorption feature in red as well as minimum wavelength mapping (MWM) of carbonate absorption features at 2335 nm in blue. Selected area for RPAS-based survey encircled in black.

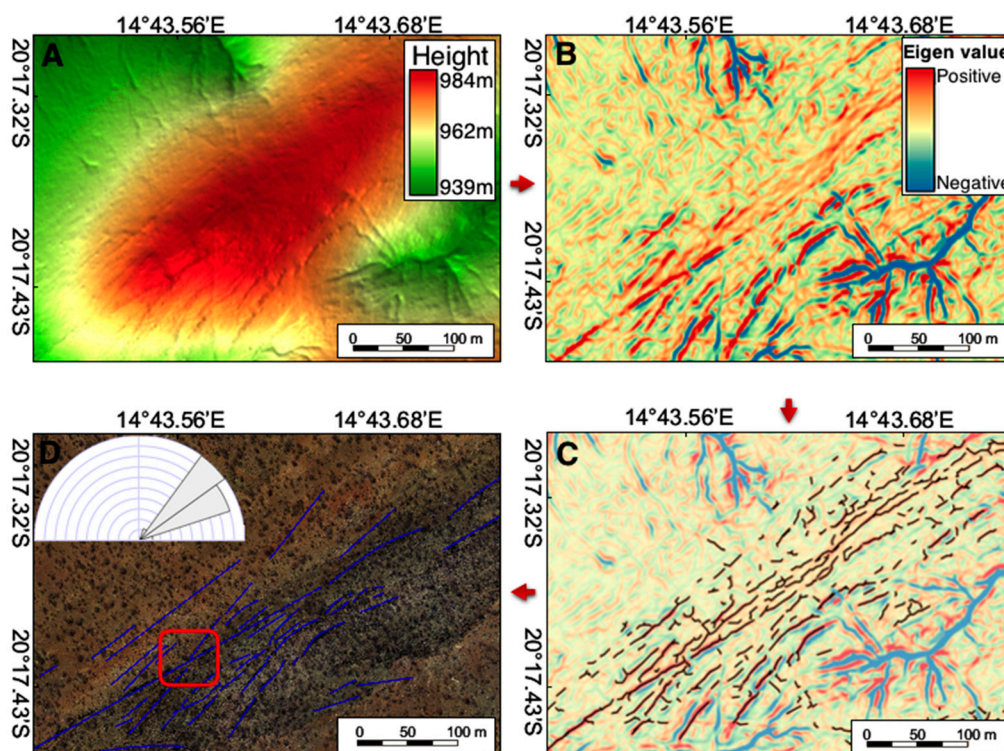


Figure 11. Flow diagram showing the process of topographical analysis. (A) High-resolution DEM derived from photogrammetry. (B) Maximum magnitude of eigenvectors (positive for ridges and negative for valleys). (C) Automatic extracted linear features (after applying a buffer around gullies). (D) Resulting interpretation of the dykes and directional Rose diagram; encircled area is the focus of the RPAS-based hyperspectral imaging.

Table 3. Steps for DEM analyses of feature extraction.

Steps	Method	Parameters
1: Resampling	Spline interpolation	Order = 3 Factor = 0.5
2: Eigen Analysis	Gaussian Filter	Sigma = 10
3: Extraction of ridges	Local Maxima	Threshold = 75%
4: Vectorization of Ridges	Minimum Segment length Minimum triangles area	Threshold = 20 pixels Threshold = 2 square pixels

We identified two types of dykes (D1 and D2) in the Rikola scene (Figure 12A), based on geometrical and compositional characteristics. The high spatial resolution data indicates that the dykes have two main orientations. One set of dykes strikes at $\sim 35^\circ$ NE (D1), whereas the other trends around 60° NE (D2). D2 cross-cut D1 creating a sinistral offset in D1 by ~ 2 m. This allows us to establish the age relationship between the two dykes (i.e., D1 intruded before D2) and thus infer that the area has at least two generations of dyke intrusions. A band ratio to enhance the iron feature on the hyperspectral data confirmed the field observation that D1 is relatively enriched in iron compared to D2 (Figure 12B). An accuracy assessment was performed to quantitatively assess the classification of the iron-rich dyke on the hyperspectral RPAS-based imagery. The image was grouped into three classes; iron-rich zones, iron-poor zones, and soil. A confusion matrix shows that the overall accuracy of the dyke classification with the iron band ratio was 84%. Moreover, the band ratio classified 81.78% of the pixels correctly and only 3.52% pixels were incorrectly classified as the iron-poor dyke and 11.54% of the pixels were mistakenly classified as soil. Most of the pixels incorrectly classified using the iron band ratio can be attributed to the numerous rock pieces and weathered surfaces surrounding the dikes. Additionally, extended limestone dissolutions and downslope precipitations were identified during our field observations. However, with these accuracies we are confident in using an iron band ratio to differentiate the dykes. Moreover, we can use their specific geometry in addition to the iron content and extend the mapping of these carbonatite dykes over the entire region.

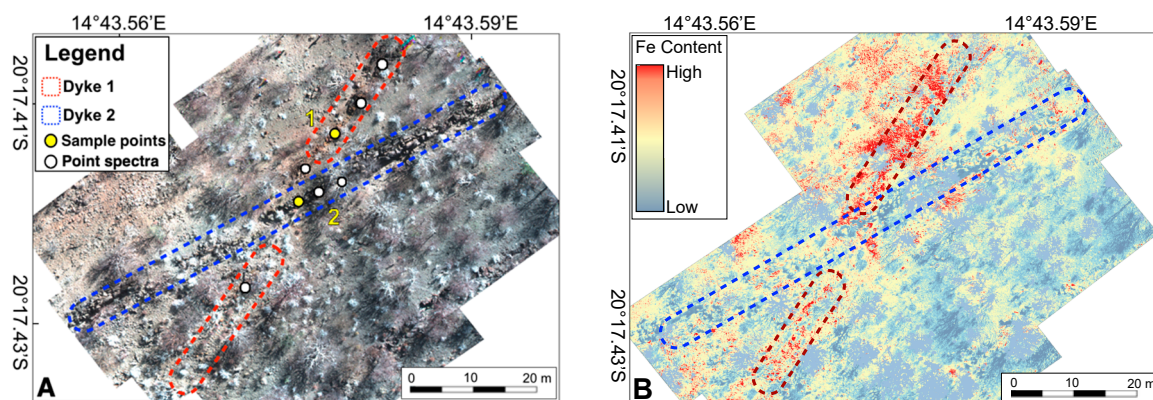


Figure 12. (A) RGB hyperspectral mosaic showing the two types of dykes. The locations of point spectra and rock sampling are shown. (B) Image showing the result of band ratio 760/503 enhancing the iron feature.

The band ratio result was confirmed in situ both with field spectroscopy and a portable XRF. Determining the precise geometry and relationships of the two sets of dykes is only made possible with the high spatial resolution hyperspectral RPAS-based images. XRF analyses were taken of rock samples from both types of dykes to validate the classification. The results of samples taken at the same point locations where spectral measurements were taken indicate that a representative dyke from D1 contained 21% iron (Fe) and 0.9% yttrium (Y), whereas a dyke belonging to D2 contained

2.5% Fe and 0.5% Y. From the in situ portable XRF analyses, we determined that the D1 dyke not only have higher Fe contents than D2, but also higher amounts of yttrium, a proxy for HREE in rocks [59]. We thus decided that the D1 dykes were promising targets and tested the in situ measurement of REE from RPAS in operational mode for the first time. A selected area was surveyed and the resulting data was adequately processed. In order to minimize false positives, the REE mapping was limited to the dykes and surrounding areas were masked out. The mask was based on the iron band ratio, in which the “non-iron” pixels are discarded.

In Figure 13, a segment of the iron-rich D1 dyke was chosen to demonstrate the methods we use to map REEs with hyperspectral RPAS-based imagery (Figure 13A). Overall, the distribution of pixels positively identified as REEs with MWM are disseminated throughout the dyke segment. MWM indicated a higher concentration of REEs in the middle (at point A) and upper parts of the dyke segment (Figure 13A). SAM and SID show pixels in red which are spectrally similar to REE hosting rocks. The reference spectra for both these methods were taken at points A and B on Dyke 1 and is shown in Figure 13A. The SID result shows positive pixels in the middle of the dyke section (Figure 13B), which are in the same region as the positive pixels of the MWM result. On the other hand, the SAM result showed visibly less positive pixels, but still showed a very little amount in the middle and lower parts of the dyke section (Figure 13C). The combination of all three methods provides us with possible indications of REE-rich zones within the dyke.

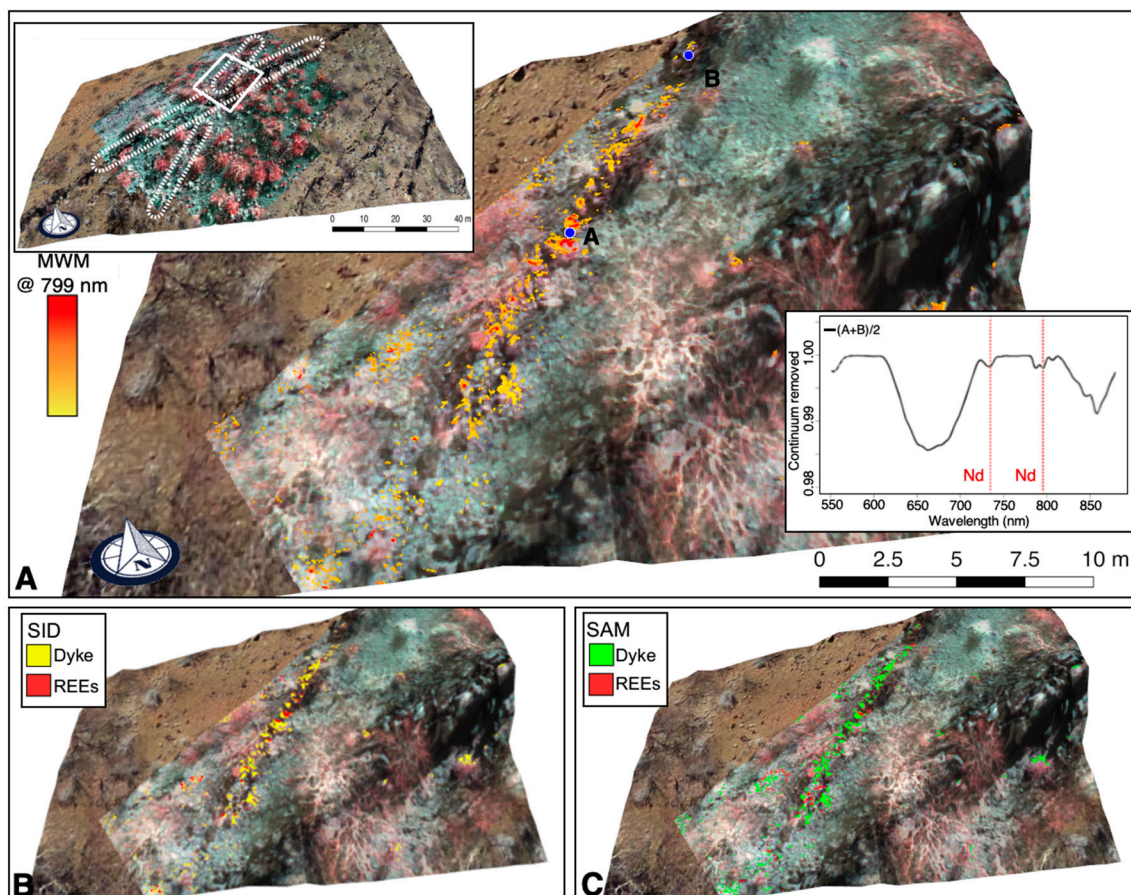


Figure 13. (A) Result of MWM on a selected section of D1 with an inset of the entire Rikola image indicating the locations of the two dykes. Pixels in red contain a deep absorption feature at 799 nm while yellow pixels do not contain an absorption feature. The displayed spectrum shows Nd absorption features, which is the result of averaging the spectra measured at points A and B and was used as reference spectra for SAM and SID. (B) SID result, indicating pixels in red as spectrally similar to REE-hosting rocks. (C) SAM result, indicating pixels in red as spectrally similar to REE-hosting rocks.

To validate our results, spectra from the hyperspectral images were compared with spectra taken by the handheld spectroradiometer of each dyke (Figure 14). Both handheld spectra show characteristic carbonate absorption features at ~2335 nm, whereas only Dyke 1 shows a broad iron charge-transfer feature in the VNIR (Figure 14A1,B1). This feature characteristically peaks at 780 nm and steeply dips from 900 nm [60]. The spectra from the Rikola range between 450 nm and 900 nm also show the iron feature in Dyke 1 (Figure 14A2,B2).

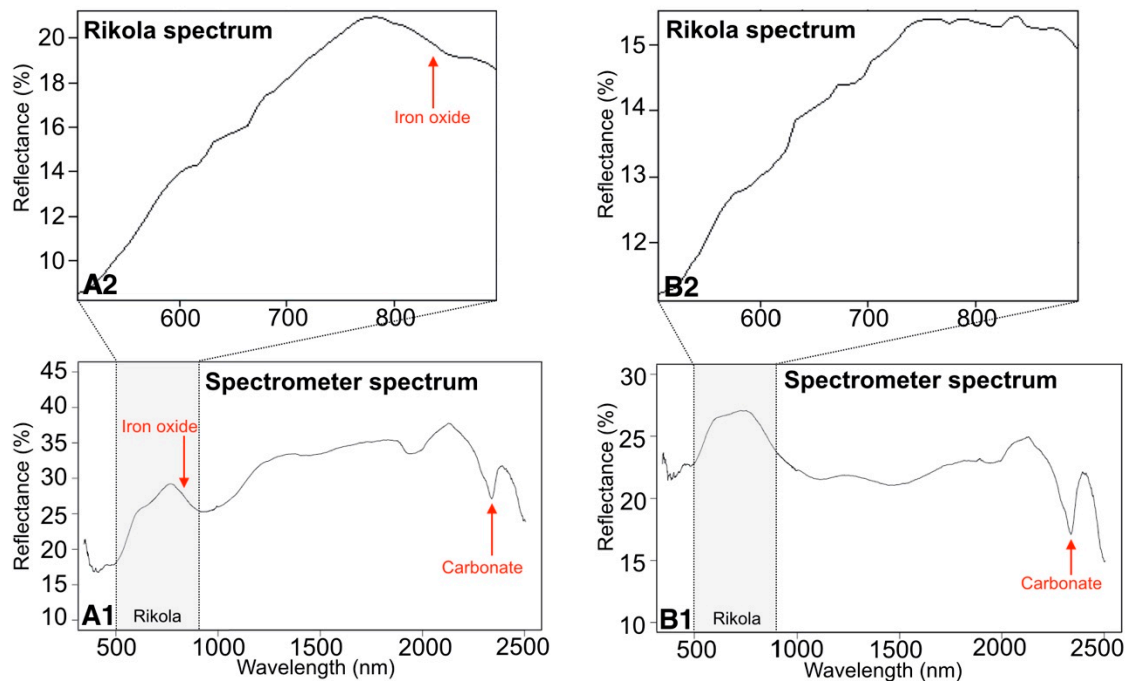


Figure 14. Diagram showing spectra taken by the portable spectrometer compared with spectra taken by the Rikola of D1 and D2 at validation points 1 and 2 respectively. (A1) Spectrometer spectrum of Dyke 1 showing a carbonate absorption feature as well as an iron oxide feature. (A2) Rikola spectrum of Dyke 1 at the same point also showing an iron oxide feature. (B1) Spectrometer spectrum of Dyke 2 showing a carbonate absorption feature. (B2) Rikola spectrum of Dyke 2 at same point.

XRD revealed that iron is mainly present in the form of goethite (FeOOH) and to lower contents as hematite (Fe₂O₃—below 3 wt-% in total). In contrast, no typical Fe-mineral was detected in the sample of Dyke 2, with the exception of a low content of chlorite. The XRD results also indicated that the samples from Dyke 1 and Dyke 2 contained 64% and 85% calcite, respectively (Tables 4 and 5), confirming that both dykes are indeed carbonatites. Both dykes contained REE-bearing minerals such as apatite and xenotime, whereas the sample from Dyke 1 contained more xenotime, one of the major REE-bearing minerals. The XRD results also confirms the in situ measurements from the portable XRF.

Table 4. XRD results of field sample taken from D1 at validation point 1 shown in Figure 12A.

Mineral: Sample NA_16-20-RB-1	Sum of Value (wt-%): Total	ESD (3sigma)
Quartz	9.4	0.2
Calcite	63.9	0.6
Hematite	2.8	0.3
Goethite	20.0	0.5
Synchysite	1.1	0.2
Thorite	0.9	0.1
Xenotime	2.0	0.2
Sum	100.1	-

Table 5. XRD results of field sample taken from D2 at validation point 2 shown in Figure 12A.

Mineral: Sample NA_16-20-RB-2	Sum of Value (wt-%): Total	ESD (3sigma)
Quartz	1.5	0.1
Calcite	84.9	0.4
Apatite	11.6	0.3
Chlorite	<2	-
Xenotime	<1	-
Sum	100.0	-

The whole rock geochemical analysis of the two samples shows similar results: Dyke 1 is more enriched in iron and REEs, especially HREEs, than Dyke 2 (Figures 15 and 16). This verifies the XRD results (with higher contents of xenotime in Dyke 1) as well as the in situ handheld XRF measurements, which also indicated that Dyke 1 has a higher amount of Y. The data from geochemical and mineralogical (XRD) investigation are consistent and support the field work and remote sensing findings.

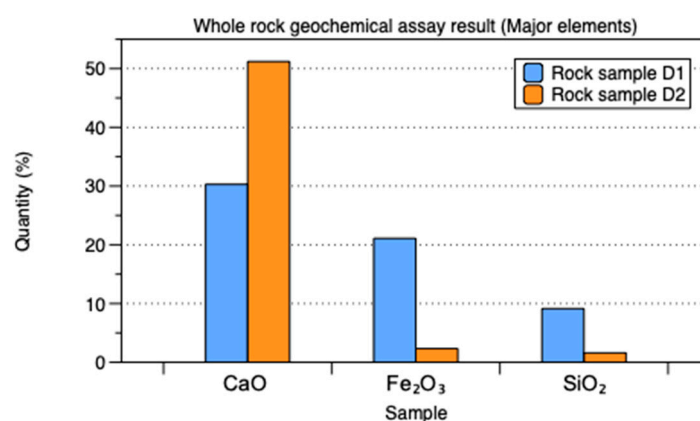


Figure 15. ICP-MS results of the rock samples taken in the field from both types of dykes; D1 and D2. Graph showing the highest amounts of major elements within each rock sample. Dyke 1 contains a higher amount of iron but less calcium than Dyke 2.

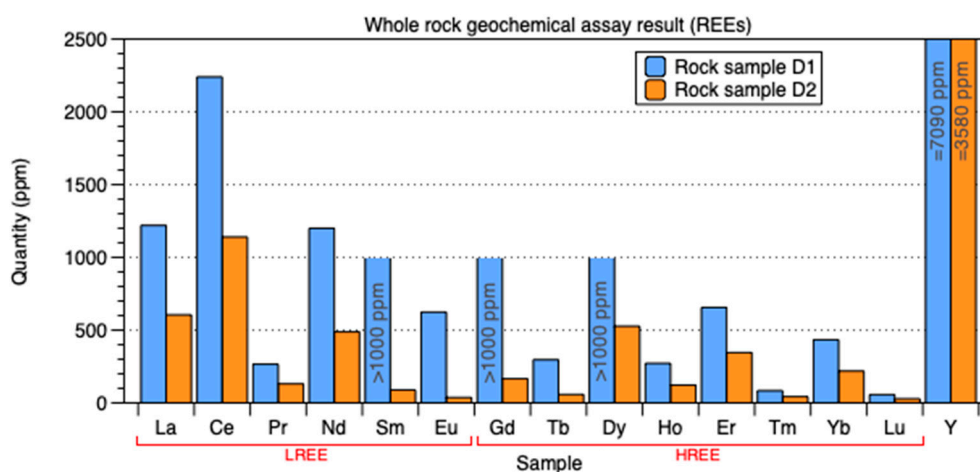


Figure 16. ICP-MS results of the rock samples taken in the field from both types of dykes; D1 and D2. Graph showing the amount of REEs within each rock sample. Dyke 1 has a higher concentration of REEs than Dyke 2.

5. Discussion

The sequence of exploration phases typically progresses from a large area to a small focused target. The integration of remote sensing data sets from different scales mirrors this fundamental

process. REE deposits associated with alkaline carbonatite complexes are typically associated with a particular magmatic or magmatic-hydrothermal phase, which affects a significantly smaller area than the whole of the complex. The first step is to identify the carbonatite–alkaline complex, where the final result should reveal a focused target for drilling and detailed sampling prior to the evaluation of the resource. The aim of an exploration geologist is to have as much information as possible about the geology of the area before doing the field work, usually in the form of a detailed geological map. Satellite and aircraft-based remote sensing is usually the first step in any field exploration endeavor, as it provides basemaps that can be used to improve or generate geological maps. Traditional geological maps in former years are usually produced through field mapping (e.g., mapping on foot) and incorporates assumptions to fill in the blanks that were based on the accepted paradigms at the times of their production. Extensive mapping is usually required in mineral exploration, especially in remote locations, where existing geological maps are imprecise and in need of upgrading.

The discovery of mineral resources in remote regions and/or without conspicuous surface indicators presents a challenge for exploration. Rare earth deposits are often associated with small-scale, lithologic (e.g., carbonatites), and tectonic structures (e.g., shear zones), and are not easily detected by traditional remote sensing. While remote sensing has been increasingly used in recent years in the field of geology thanks to the development of better sensors (multi- and hyperspectral, and airborne and satellite-based) and increased computing power [61], it is not commonly and operatively used in mineral exploration. In this manuscript we argue that multiscale remote sensing approaches provide a cost effective way of exploring critical metals hosted in poorly accessible structures. We also demonstrate that field mapping and sampling with prior remote sensing is often efficient and more lucrative.

Previously, the use of remote sensing in the field of earth observation has focused more on the agricultural and environmental sectors. Topics such as precision farming [62,63] and environmental monitoring [64,65] have long dominated the remote sensing field. Lesser focus has been placed on the geological application of remote sensing. That being said, a few studies have successfully mapped large geological features via multispectral and/or hyperspectral satellite sensors, providing large scale estimates of the area in question [47,61,66]. The challenging aspect for researchers at the moment is the resolution gap between satellite- or aircraft-based imaging, and ground surveying. To address this challenge, an innovative approach is taken whereby RPAS are used to bridge the gap in the scale of data collection. This study not only uses one type of sensor and data scale, but introduces a work scheme involving various data sources, from satellite- and aircraft-based, to RPAS-based sensors and ground-based surveys. The work chain is then completed with field validation through geochemical and spectral analyses.

We used ASTER and HyMap data in combination with existing geological maps to improve field exploration and rock sampling and identify areas of interest. We were able to map the regional geology and major structures with band ratios using satellite data. Additionally, ASTER-TIR data can be used to map felsic rocks, such as the syenites we investigated in this study. Ratios such as a quartz index have been shown to be valuable tools in determining the locations of felsic rocks covering large area extents [67]. The major structures we mapped shows that large scale deformation took place and indicate that the area might have undergone hydrothermal activity. With this information we were able to locate a promising region of interest for the exploration of REE-hosted carbonatites. The spectrally and spatially higher resolution HyMap data allowed us to further analyze the area by identifying regions of overlapping carbonate and iron features and, thus, select a particular region of interest. Selecting the relevant samples was made possible with an improved geological map and by identifying the relevant areas anteriorly, decreased the amount of required samples. Ultimately, field work was improved, accelerated and simplified.

Currently, RPAS are mainly used for SfM-MVS photogrammetry and aerial photography. Studies such as mine and tailings monitoring [68,69], glaciology, and land slide monitoring [70–72], as well as topographic mapping [73], have largely used RPAS for SfM-MVS purposes and aerial photography. Hyperspectral RPAS-based surveying is still a new and developing field, and has almost primarily

been used in precision agriculture and forestry [17,21,74]. There are however a few studies which uses hyperspectral RPAS-based surveying for environmental monitoring, such as the impact mining has on the environment [50]. Nonetheless, the use of RPASs for mineral exploration is an underutilized source for data acquisition. For this study we attempt to use the full potential of RPAS-based imaging. We not only use topographic information captured with RPAS, but we integrate it with spectral information from a hyperspectral RPAS-based sensor. Topographic information from RPAS-based data was used to automatically map the dykes in the area. This data was obtained through SfM-MVS photogrammetry using the fixed-winged eBee. As the eBee is able to cover 4 sq.km/hour, the majority of the dykes in Area 1 could be mapped in 20 min, and the processing time for the data takes a few hours. Traditional field mapping of the same area would have taken a geologist days. Altogether, this technique is much faster, safer and the procedure is cheaper than conventional field mapping.

During the field campaign, we selected promising areas and tested the detection of REEs from RPAS directly in the field for the first time. The RPAS-based Rikola data showed that it is possible to distinguish different types of dykes based on their iron content. Additionally, the high spatial resolution of the data made it possible to determine the age relationship between the dykes based on their positions to each other. Identifying REEs within an individual dyke has proven to be challenging. Ideally, MWM would have been the most direct method to map REEs, but noise introduced by RPAS-based imaging created uncertainties. Thus, to tackle this challenge, we used spectral classification methods as well, and we were able to adequately pinpoint possible REE enriched zones within a dyke by comparing all three results. Field validation is essential for the study of mineral exploration with remote sensing data. Each carbonatite body studied by means of satellite-, aircraft-, and RPAS-based surveys required proper geochemical validation. To validate the remote sensing data, rock samples were collected in the field for laboratory geochemical and spectral analyses. By determining the iron content of rock samples from each dyke with whole rock geochemical analyses and XRF, we validated the procedure to spectrally classify dykes based on iron content. Geochemical analyses also indicated that there were in fact more HREE in the iron-rich dykes, which focused our attentions on one set of dykes, increasing the efficiency of our investigations. Being able to successfully validate the remote sensing results demonstrates that our multisource approach to mineral exploration can easily be extended to other structurally bound deposits.

This study has integrated and synthesized information from multiple platforms with diverse sensors to provide improvements to the detection of REE mineralization within structurally bound carbonatite bodies. Although mapping of wide areas can be done with satellite acquisitions, it lacks the spatial resolution required to identify small structures. Thus, aircraft- and RPAS-borne sensors are used additionally to obtain data with an increased spatial resolution over a smaller, more defined area. Although we focus on the remote sensing aspects, it is not intended to replace traditional exploration procedures but rather to improve them. When taking costs into consideration, based on our previous experience, RPAS-based surveys usually become considerably cheaper beyond approximately nine days of field mapping by a qualified geologist. This calculation is based on logistical (e.g., import/export and transport) and operational (e.g., processing) factors and might slightly vary depending on the local conditions (e.g., remoteness and accessibility).

On the other hand, the use of RPASs for mineral exploration purposes does have a few challenging aspects. Environmental factors such as strong winds and bad weather conditions may prohibit the RPAS from flying. All these challenges however can be overcome with diligent flight planning. Hyperspectral RPAS-based surveying is still a developing field. This means that there are no standardized preprocessing methods universally used for the acquired data. It is, therefore, very important to practice verified preprocessing procedures to ensure well-corrected, quality data [75]. Furthermore, our data processing workflow can be adapted to other deposits and is not limited to carbonatite-hosted REEs. It can be adjusted to detect deposits associated with alteration or deposits characterized by specific structures and geometries.

This approach can greatly improve exploration targeting for various commodities. By no means does this technique replace geologists in the field. With this approach we intended to improve traditional exploration methods by (1) reducing the exploration footprint, (2) increasing personal safety, as well as (3) accelerating the overall process.

6. Conclusions and Outlook

Multisource and multiscale field exploration integrates the full range of available remote sensing data sets, from space-borne imaging over airborne data, to high-resolution RPAS-based hyperspectral data acquisition as well as ground validation. These diverse data sets provide indispensable information on the relief and mineral contents of the geological formations in areas of interest at different scales. However, spectral data alone can lack the sufficient discrimination potential either due to spatial and spectral sensor resolutions or noise produced during acquisition. The integration of geomorphic data can improve mapping. It is also important to have an accurate preprocessing scheme for the topographic and spectral data obtained from RPAS platforms. We demonstrated that our correction methods produced geometrically and spectrally accurate results. The use of RPAS-based exploration in the chain of multisource and multiscale data acquisition resulted in data with both high spectral and spatial resolution. Despite the fact that the use of RPAS in the field is not always possible due to environmental factors, RPAS- and/or ground-based surveying lowers the costs and improves the accuracy of field data, which shows its high potential in the use of future mineral exploration.

In the case of carbonatite hosted REEs in southern Africa we could demonstrate that: (1) Multispectral satellite data can be used for regional scale targeting and structural interpretation. (2) The high spatial resolution from hyperspectral airplane-based data can allow us to locate regions of interest for further high resolution mapping. (3) High spatial resolution imagery captured with RPAS allowed us to study and map relatively small sized structures, and (4) by using high spatial resolution RPAS-based hyperspectral data we could identify promising areas with high REE concentrations. Based on the above findings, we suggest that a multisource and multiscale approach is beneficial for the exploration of structurally bound mineral deposits.

One current limitation is that the spectral range of low-cost, lightweight RPAS-based cameras only cover the visible and NIR part of the spectrum. This makes it impossible to detect important absorption features situated in the SWIR portion of the electromagnetic spectrum. However, with the rapid pace of technological advancements, it is only a matter of time when such a sensor will be developed. Additionally, RPAS-based magnetometers may offer subsurface solutions which can be integrated with surficial mineral mapping from hyperspectral RPAS-based data. These technologies will probably revolutionize the field of remote sensing geology.

Author Contributions: Conceptualization, R.B., R.G., and R.Z.; Methodology, R.B., R.G., S.L., R.Z., L.A., and R.M.; Formal Analysis, R.B., R.G., S.L., R.Z., L.A., and R.M.; Investigation, R.B., R.G., R.Z., S.L., and P.A.M.N.; Writing—Original Draft Preparation, all authors; Writing—Review & Editing, all authors; Visualization, R.B., R.G. and S.L.; Supervision, R.G. and P.A.M.N.; Project Administration, R.G., R.B., R.Z., and P.A.M.N.

Funding: This research received no external funding.

Acknowledgments: The Helmholtz Institute Freiberg for Resource Technology a division of the Helmholtz-Zentrum Dresden-Rossendorf (HZDR) together with the University of the Witwatersrand is thanked for the support and funding of this project. We would like to gratefully thank the Namibian Rare Earths Inc. team, specifically, geologist Bonaface Katanga, for access and showing us around Lofdal, as well as sharing their data and insights into the area. We would also like to thank the Geological Survey of Namibia, specifically Kombada Mhopjeni the deputy director (Geo-Information), for logistical support and data sharing.

Conflicts of Interest: The authors declare no conflicts of interest.

Appendix A. Preprocessing of RPAS-Based Data

SfM-MVS is a low-cost, user-friendly workflow combining photogrammetric techniques, 3D computer vision, and conventional surveying techniques. It solves the equations for camera pose and scene geometry automatically using a highly redundant bundle adjustment [76,77]. SfM-MVS

benefits from a moving platform in order to acquire numerous RGB pictures, from varying angles and with sufficient overlap to compute a digital surface model (DSM). Surface geometry is reconstructed using a SfM-MVS workflow as outlined in Carrivick et al. [78] and James et al. [79] in Agisoft PhotoScan Professional 1.2.5. Processing parameters are set to “high quality” for image alignment at reference tie point selection. Blurred images and those with high residual keypoint errors are excluded from further dense cloud matching. Prior to dense cloud reconstruction at “high quality” with depth filtering set to “aggressive”, outlier tie points are removed using the gradual selection tool. The workflow used in this study consisted of eight steps:

- Step (1): Detection of characteristic image points.
- Step (2): Followed by automatic point matching using a homologous transformation.
- Step (3): Keypoint filtering. This step is crucial for model accuracy and validation for later results.
- Step (4): Iterative bundle adjustment to reconstruct the image acquisition geometry and internal camera parameters.
- Step (5): Scaling and georeferencing of the intrinsic coordinate system to available reference points (GCPs) or camera coordinates and optimisation of the resulting sparse cloud.
- Step (6): Applying Multi-View Stereo algorithms (dense matching) to compute the dense cloud. This resulting dense cloud is basis for the projection of the hyperspectral data into 3D.
- Step (7): Interpolation of the dense cloud by, e.g., either Meshing or Inverse Distance Weighting (IDW), to retrieve a Digital Surface Model (DSM).
- Step (8): Texturising the 3D model.

RPAS-based hyperspectral data were acquired with an Aibotix Aibot X6v2 hexacopter. The hexacopter has a maximum flight time of 15 min and a built-in GPS. Hyperspectral data were captured by the Rikola Hyperspectral Imager. Camera and data parameters are summarized in Table 2 [80]. A pre-defined flight plan is uploaded to attain a minimum image overlap of 20%. HSI data receive a position stamp using the built-in navigation GPS receiver and are calibrated using a relative irradiance sensor.

A specific sequence of preprocessing corrections are required for RPAS-borne hyperspectral imaging in order to transform the raw data to calibrated and, thus, usable hyperspectral datacubes [28]. The raw data is preprocessed and calibrated using the MEPHySto toolbox [28]. The preprocessing workflow is as follows.

1. Conversion to Radiance: The first step in the preprocessing chain is to perform a dark current subtraction on each image separately; this is done with the software provided by Rikola Ltd. A dark frame captured by the camera is subtracted from each image frame to correct for the dark current component of the sensor. With additional vignetting and sensor-specific corrections, the provided software then converts the raw digital numbers to radiance.
2. Lens correction and co-registration: Image deformations caused by internal camera features such as characteristic lens distortions need to be corrected. These steps are done with the MEPHySto toolbox. The toolbox also co-register the spectral bands with one another. This spatial shift occurs between single bands due to small temporal gaps that occur during image capturing while the sensor is moving.
3. Orthorectification and georeferencing: The images can then be automatically orthorectified and georeferenced by the toolbox. Detection of local features or “keypoints” is performed with a SIFT algorithm. A point matching algorithm is then used to match points between the hyperspectral image and a geographically corrected orthophoto produced by SfM-MVS photogrammetry. In the current study, the hyperspectral images were manually georeferenced instead. The high abundance of leafless trees in the study area led to notable differences between related image pairs even at slightly differing viewing angles, which makes the successful matching of key points extremely difficult and inhibits image pairing. The high similarity of the trees in shape and

size additionally creates strong geometric patterns and thus impedes the detection of individual invariants. Therefore, manual georeferencing was applied in QGIS open-source software before further processing.

4. Topographic correction: The relief of the area, such as slopes in various orientations with respect to sun incidence, influences the illumination within an image. Different sunlight incidence angles on the same material cause the radiance of that material to vary. The MEPHySTo toolbox may be used to perform respective topographic corrections. In this case, topographic correction was performed but did not provide any additional improvement therefore both corrected and uncorrected data can be used further. For this study case, uncorrected data was used in preference as topographic correction can introduce artifacts that affect the spectral content if the noise in the DEM is large compared to the relief in the scene.
5. Radiometric correction: The hyperspectral radiance images are converted to reflectance using an empirical line correction. This is done by using known spectra from black, gray, and white PVC panels placed in the field while the images are being captured.
6. Spectral smoothing: A Savitzky–Golay filter was used to smooth the data to decrease spectral noise. A successive series of low degree polynomials is fitted to each hyperspectral spectrum using linear least squares within a defined moving window (Savitzky & Golay 1964). A polynomial order of 3 was chosen with a window size of 5.
7. Mosaicking: As a last step, the corrected and georeferenced images can be stitched together to create a mosaic of the entire area.

Appendix B. Suitability of the Rikola Imager

The first question that comes to mind concerning the potential of a lightweight hyperspectral imager for operational use is if the spectral resolution and SNR of the Rikola imager is sufficient for the direct detection of REEs. The Rikola imager was thus initially tested in the laboratory to capture hyperspectral images of cut samples to validate the use of the device in operational conditions.

Cut samples allow the capture of spectra on a clean, unweathered surface to produce accurate spectral results. We stacked multiple acquisitions and averaged them to eliminate noise without erasing minute spectral features and thus produce a robust and reliable spectrum. A selected spectrum was compared with a spectrum taken by a portable spectrometer on the same point on the sample (Figure A1). Nd absorption features can be seen in the spectrum from the Rikola and from the spectrometer. The slight shift in the observed Rikola spectrum (~7 nm shift to higher wavelength) can be attributed to the varying spectral resolutions of the two sensors in the device. This sampling effect generates a bias in the discrimination on the local minima that can reach up to half the spectral resolution. It should be noted that the shift might also be attributed to the insufficient spectral calibration of the sensor. It is also worth noting the section of the Rikola spectrum labeled as sensor noise in Figure A1 is caused by the internal setup of the camera. The camera consists of 2 sensors, one captures spectra from 506–636 nm while the other sensor captures the VNIR range from 650 to 900 nm [81]. This causes a spectral jump in the range of ~640 nm (between the spectral ranges of the two sensors), but does not affect the rest of the spectrum in any way. The laboratory test confirms that the Rikola camera can detect REEs under laboratory conditions. We, therefore, concluded that it could be possible to identify REE signatures in field conditions.

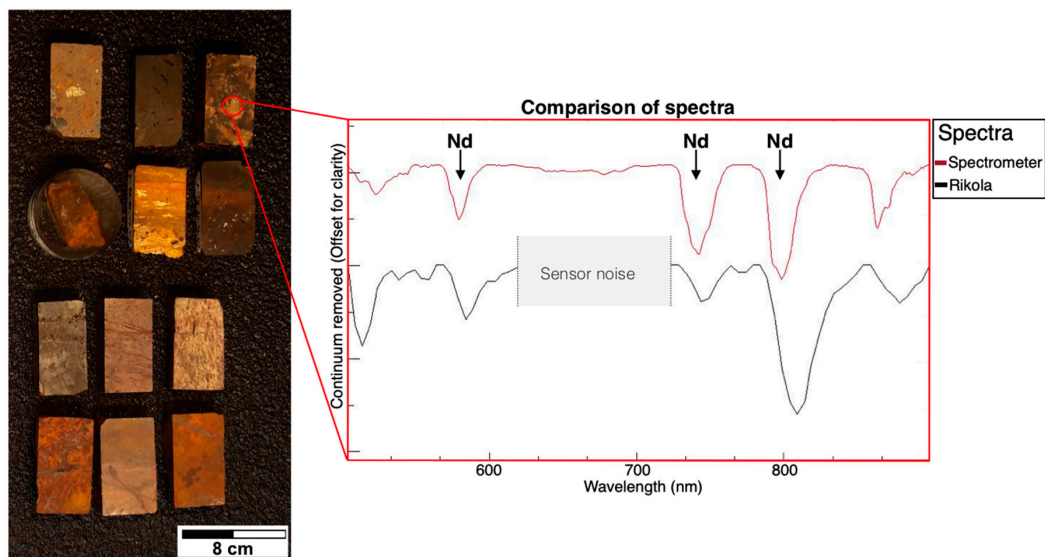


Figure A1. Spectrum taken from a Rikola image of rock samples from the field, compared with spectrum taken of the same sample with the spectrometer. Nd absorption features can be seen in both spectra at the same wavelengths.

References

1. Simandl, G.J. Geology and market-dependent significance of rare earth element resources. *Mineral. Depos.* **2014**, *49*, 889–904. [[CrossRef](#)]
2. Boesche, N.K.; Rogass, C.; Lubitz, C.; Brell, M.; Herrmann, S.; Mielke, C.; Tonn, S.; Appelt, O.; Altenberger, U.; Kaufmann, H. Hyperspectral REE (rare earth element) mapping of outcrops-applications for neodymium detection. *Remote Sens.* **2015**, *7*, 5160–5186. [[CrossRef](#)]
3. Neave, D.A.; Black, M.; Riley, T.R.; Gibson, S.A.; Ferrier, G.; Wall, F.; Broom-Fendley, S. On the feasibility of imaging carbonatite-hosted rare earth element deposits using remote sensing. *Econ. Geol.* **2016**, *111*, 641–665. [[CrossRef](#)]
4. Simandl, G.J.; Paradis, S. Carbonatites: Related ore deposits, resources, footprint, and exploration methods. *Appl. Earth Sci.* **2018**, *127*, 123–152. [[CrossRef](#)]
5. Van der Meer, F. Analysis of spectral absorption features in hyperspectral imagery. *Int. J. Appl. Earth Obs. Geoinf.* **2004**, *5*, 55–68. [[CrossRef](#)]
6. Turner, D.J.; Rivard, B.; Groat, L.A. Visible and short-wave infrared reflectance spectroscopy of REE phosphate minerals. *Am. Mineral.* **2016**, *101*, 2264–2278. [[CrossRef](#)]
7. Rowan, L.C.; Kingston, M.J.; Crowley, J.K. Spectral reflectance of carbonatites and related alkalic igneous rocks: Selected samples from four North American localities. *Econ. Geol.* **1986**, *81*, 857–871. [[CrossRef](#)]
8. Rockwell, B.W.; Hofstra, A.H. Identification of quartz and carbonate minerals across northern Nevada using aster thermal infrared emissivity data-implications for geologic mapping and mineral resource investigations in well-studied and frontier areas. *Geosphere* **2008**, *4*, 218–246. [[CrossRef](#)]
9. Castaldi, F.; Palombo, A.; Santini, F.; Pascucci, S.; Pignatti, S.; Casa, R. Evaluation of the potential of the current and forthcoming multispectral and hyperspectral imagers to estimate soil texture and organic carbon. *Remote Sens. Environ.* **2016**, *179*, 54–65. [[CrossRef](#)]
10. Kruse, F.A.; Boardman, J.W.; Huntington, J.F. Comparison of airborne hyperspectral data and EO-1 Hyperion for mineral mapping. *IEEE Trans. Geosci. Remote Sens.* **2003**, *41*, 1388–1400. [[CrossRef](#)]
11. Cocks, T.; Jenssen, R.; Stewart, A.; Wilson, I.; Shields, T. The HyMap TM airborne hyperspectral sensor: The system, calibration and performance. In Proceedings of the 1st EARSel workshop on Imaging Spectroscopy, Zurich, Switzerland, 6–8 October 1998; pp. 37–42.
12. Zimmermann, R.; Brandmeier, M.; Gloaguen, R. Possibilities and challenges of remote sensing for exploration of Geological setting and reference dataset. In Proceedings of the IAMG, Annual Conference of the International Association for Mathematical Geosciences, Freiberg, Saxony, Germany, 5–13 September 2015; pp. 773–783.

13. Zimmermann, R.; Brandmeier, M.; Andreani, L.; Mhopjeni, K.; Gloaguen, R. Remote sensing exploration of Nb-Ta-LREE-enriched carbonatite (Epembe/Namibia). *Remote Sens.* **2016**, *8*, 11–17. [[CrossRef](#)]
14. Othman, A.A.; Gloaguen, R. Improving lithological mapping by SVM classification of spectral and morphological features: The discovery of a new chromite body in the Mawat ophiolite complex (Kurdistan, NE Iraq). *Remote Sens.* **2014**, *6*, 6867–6896. [[CrossRef](#)]
15. Honkavaara, E.; Hakala, T.; Kirjasniemi, J.; Lindfors, A.; Nurminen, K.; Ruokokoski, P.; Saari, H.; Markelin, L. New Light-Weight Stereoscopic Spectrometric Airborne Imaging Technology for High-Resolution Environmental Remote Sensing—Case Studies in Water Quality Mapping. *Int. Arch. Photogramm. Remote Sens. Spat. Inf. Sci.* **2013**, *XL-1/W1*, 21–24. [[CrossRef](#)]
16. Hunt, E.R.; Dean Hively, W.; Fujikawa, S.J.; Linden, D.S.; Daughtry, C.S.T.; McCarty, G.W. Acquisition of NIR-green-blue digital photographs from unmanned aircraft for crop monitoring. *Remote Sens.* **2010**, *2*, 290–305. [[CrossRef](#)]
17. Colomina, I.; Molina, P. Unmanned aerial systems for photogrammetry and remote sensing: A review. *ISPRS J. Photogramm. Remote Sens.* **2014**, *92*, 79–97. [[CrossRef](#)]
18. Turner, D.; Lucieer, A.; Malenovský, Z.; King, D.H.; Robinson, S.A. Spatial co-registration of ultra-high resolution visible, multispectral and thermal images acquired with a micro-UAV over antarctic moss beds. *Remote Sens.* **2014**, *6*, 4003–4024. [[CrossRef](#)]
19. Honkavaara, E.; Saari, H.; Kaivosoja, J.; Pölonen, I.; Hakala, T.; Litkey, P.; Mäkynen, J.; Pesonen, L. Processing and assessment of spectrometric, stereoscopic imagery collected using a lightweight UAV spectral camera for precision agriculture. *Remote Sens.* **2013**, *5*, 5006–5039. [[CrossRef](#)]
20. Salami, E.; Barrado, C.; Pastor, E. UAV flight experiments applied to the remote sensing of vegetated areas. *Remote Sens.* **2014**, *6*, 11051–11081. [[CrossRef](#)]
21. Costa, F.G.; Ueyama, J.; Braun, T.; Pessin, G.; Osório, F.S.; Vargas, P.A. The use of unmanned aerial vehicles and wireless sensor network in agricultural applications. In Proceedings of the 2012 IEEE International Geoscience and Remote Sensing Symposium, Munich, Germany, 22–27 July 2012; pp. 5045–5048.
22. Rufino, G.; Moccia, A. *Integrated VIS-NIR Hyperspectral/Thermal-IR Electro-Optical Payload System for a Mini-UAV*; Infotech@Aerospace: Arlington, VA, USA, 2005; p. 7009.
23. Candiago, S.; Remondino, F.; De Giglio, M.; Dubbini, M.; Gattelli, M. Evaluating multispectral images and vegetation indices for precision farming applications from UAV images. *Remote Sens.* **2015**, *7*, 4026–4047. [[CrossRef](#)]
24. Salati, S.; Van Ruitenbeek, F.; Van der Meer, F.; Naimi, B. Detection of alteration induced by onshore gas seeps from ASTER and worldview-2 Data. *Remote Sens.* **2014**, *6*, 3188–3209. [[CrossRef](#)]
25. McDowell, M.L.; Bruland, G.L.; Deenik, J.L.; Grunwald, S.; Knox, N.M. Soil total carbon analysis in Hawaiian soils with visible, near-infrared and mid-infrared diffuse reflectance spectroscopy. *Geoderma* **2012**, *189*, 312–320. [[CrossRef](#)]
26. Bhatti, A.M.; Rundquist, D.; Schalles, J.F.; Steele, M.; Takagi, M. Qualitative Assessment of Inland and Coastal Waters By Using. *Int. Arch. Photogramm. Remote Sens. Spat. Inf. Sci. Part 8 Kyoto Japan* **2010**, *38*, 415–420.
27. Lorenz, S.; Salehi, S.; Kirsch, M.; Zimmermann, R.; Unger, G.; Sørensen, E.V.; Gloaguen, R. Radiometric correction and 3D integration of long-range ground-based hyperspectral imagery for mineral exploration of vertical outcrops. *Remote Sens.* **2018**, *10*, 176. [[CrossRef](#)]
28. Jakob, S.; Zimmermann, R.; Gloaguen, R. The Need for Accurate Geometric and Radiometric Corrections of Drone-Borne Hyperspectral Data for Mineral Exploration: MEPHySTo-A Toolbox for Pre-Processing Drone-Borne Hyperspectral Data. *Remote Sens.* **2017**, *9*, 88. [[CrossRef](#)]
29. Siegfried, P.; Hall, M. *NI 43–101 Technical Report and Mineral Resource Estimate for Area 4 of the Lofdal Rare Earth Element (REE) Project*; Khorixas District, Republic of Namibia, The MSA Group (Pty) Ltd.: Randburg, Gauteng, South Africa, 2012.
30. Namibia Rare Earths Inc. *Preliminary Economic Assessment Confirms Potential for Heavy Rare Earth Mine at Lofdal: Press Release*; InvestorIntel Corp.: New York, NY, USA, 2014; Volume 25.
31. Williams-Jones, A.E.; Wollenberg, R.; Bodeving, S. Hydrothermal fractionation of the rare earth elements and the genesis of the Lofdal REE deposit, Namibia. *Geol. Surv. Pap.* **2015**, *3*, 125–130.
32. Do Cabo, V.N. Geological, Mineralogical and Geochemical Characterisation of the Heavy Rare Earth-rich Carbonatites at Lofdal, Namibia. Ph.D. Thesis, University of Exeter, Exeter, UK, 2013.

33. Kaul, A. A Petrological Study of REE-Rich Carbonatite Intrusions from the Lofdal Farm Area, Namibia, Africa. Bachelor's Thesis, Acadia University, Wolfville, NS, Canada, 2010.
34. Jung, S.; Hoffer, E.; Hoernes, S. Neo-Proterozoic rift-related syenites (Northern Damara Belt, Namibia): Geochemical and Nd-Sr-Pb-O isotope constraints for mantle sources and petrogenesis. *Lithos* **2007**, *96*, 415–435. [[CrossRef](#)]
35. Wall, F.; Niku-Paavola, V.N.; Storey, C.; Müller, A.; Jeffries, T. Xenotime-(Y) from carbonatite dykes at Lofdal, Namibia: Unusually low LREE:HREE ratio in carbonatite, and the first dating of xenotime overgrowths on zircon. *Can. Mineral.* **2008**, *46*, 861–877. [[CrossRef](#)]
36. Bodeving, S.; Williams-Jones, A.E.; Swinden, S. Carbonate-silicate melt immiscibility, REE mineralising fluids, and the evolution of the Lofdal Intrusive Suite, Namibia. *Lithos* **2017**, *268*, 383–398. [[CrossRef](#)]
37. Andreani, L.; Stanek, K.P.; Gloaguen, R.; Krentz, O.; Domínguez-González, L. DEM-based analysis of interactions between tectonics and landscapes in the ore mountains and eger rift (East Germany and NW Czech Republic). *Remote Sens.* **2014**, *6*, 7971–8001. [[CrossRef](#)]
38. Lorenz, S.; Beyer, J.; Fuchs, M.; Seidel, P.; Turner, D.; Heitmann, J.; Gloaguen, R. The potential of reflectance and laser induced luminescence spectroscopy for near-field rare earth element detection in mineral exploration. *Remote Sens.* **2019**, *11*, 21. [[CrossRef](#)]
39. Amer, R.; Kusky, T.; Ghulam, A. Lithological mapping in the Central Eastern Desert of Egypt using ASTER data. *J. Afr. Earth Sci.* **2010**, *56*, 75–82. [[CrossRef](#)]
40. Rowan, L.C.; Mars, J.C. Lithologic mapping in the Mountain Pass, California area using Advanced Spaceborne Thermal Emission and Reflection Radiometer (ASTER) data. *Remote Sens. Environ.* **2003**, *84*, 350–366. [[CrossRef](#)]
41. Adler-Golden, S.; Berk, A.; Bernstein, L.S.; Richtsmeier, S.; Acharya, P.K.; Matthew, M.W.; Anderson, G.P.; Allred, C.L.; Jeong, L.S.; Chetwynd, J.H. FLAASH, a MODTRAN4 atmospheric correction package for hyperspectral data retrievals and simulations. *Summ. Seventh JPL Airborne Earth Sci. Work.* **1998**, *4*, 9–14.
42. Kruse, F.; Boardman, J.; Lefkoff, A.B.; Young, J.; Kierein-Young, K. HyMap: An Australian hyperspectral sensor solving global problems-results from USA HyMap data acquisitions. In Proceedings of the 10th Australasian Remote Sensing and Photogrammetry Conference, Adelaide, South Australia, Australia, 21–25 August 2000; pp. 18–23.
43. Le Bas, M.J. Fenites associated with carbonatites. *Can. Mineral.* **2008**, *46*, 915–932. [[CrossRef](#)]
44. Williams-Jones, A.E.; Palmer, D.A.S. The evolution of aqueous-carbonic fluids in the Amba Dongar carbonatite, India: Implications for fenitisation. *Chem. Geol.* **2002**, *185*, 283–301. [[CrossRef](#)]
45. Harmer, R.E.; Nex, P.A.M. Rare Earth Deposits of Africa. *Episodes* **2016**, *39*, 381–406. [[CrossRef](#)]
46. Thomas, M.; Laukamp, C.; Hewson, R.; Rodger, A. *Next Generation Mineral Mapping: Queensland Airborne HyMap and Satellite ASTER Surveys 2006–2008*; Publicly Available Report: P2007/364; CSIRO: Canberra, New South Wales, Australia, 2008.
47. Abrams, M.; Hook, S. Simulated ASTER Data 1 for Geological Studies. *IEEE Trans. Geosci. Remote Sens.* **1995**, *33*, 692–699. [[CrossRef](#)]
48. Gad, S.; Kusky, T. ASTER spectral ratioing for lithological mapping in the Arabian-Nubian shield, the Neoproterozoic Wadi Kid area, Sinai, Egypt. *Gondwana Res.* **2007**, *11*, 326–335. [[CrossRef](#)]
49. Murphy, R.J.; Monteiro, S.T. Mapping the distribution of ferric iron minerals on a vertical mine face using derivative analysis of hyperspectral imagery (430–970 nm). *ISPRS J. Photogramm. Remote Sens.* **2013**, *75*, 29–39. [[CrossRef](#)]
50. Jackisch, R.; Lorenz, S.; Zimmermann, R.; Möckel, R.; Gloaguen, R. Drone-borne hyperspectral monitoring of acid mine drainage: An example from the Sokolov lignite district. *Remote Sens.* **2018**, *10*, 385. [[CrossRef](#)]
51. Van Ruitenbeek, F.J.A.; Bakker, W.H.; Van der Werff, H.M.A.; Zegers, T.E.; Oosthoek, J.H.P.; Omer, Z.A.; Marsh, S.H.; Van der Meer, F.D. Mapping the wavelength position of deepest absorption features to explore mineral diversity in hyperspectral images. *Planet. Space Sci.* **2014**, *101*, 108–117. [[CrossRef](#)]
52. Gaffey, S.J. Spectral reflectance of carbonate minerals in the visible and near infrared (0.35–2.55 microns): Calcite, aragonite, and dolomite. *Am. Mineral.* **1986**, *71*, 151–162.
53. Kruse, F.A. Identification and mapping of minerals in drill core using hyperspectral image analysis of infrared reflectance spectra. *Int. J. Remote Sens.* **1996**, *17*, 1623–1632. [[CrossRef](#)]

54. Hecker, C.; Van der Meijde, M.; Van der Werff, H.; Van der Meer, F.D. Assessing the influence of reference spectra on synthetic SAM classification results. *IEEE Trans. Geosci. Remote Sens.* **2008**, *46*, 4162–4172. [[CrossRef](#)]
55. Chang, C.I. Spectral Information Divergence for Hyperspectral Image Analysis. In Proceedings of the IEEE 1999 International Geoscience and Remote Sensing Symposium, Hamburg, Germany, 28 June–2 July 1999; Volume 1, pp. 509–511.
56. Jin, J.; Yang, L.; Zhang, X.; Ding, M. Vascular Tree Segmentation in Medical Images Using Hessian-Based Multiscale Filtering and Level Set Method. *Comput. Math. Methods Med.* **2013**, *2013*. [[CrossRef](#)]
57. Frangi, A.F.; Niessen, W.J.; Vincken, K.L.; Viergever, M.A. Multiscale Vessel Enhancement Filtering. In Proceedings of the International Conference on Medical Image Computing and Computer-Assisted Intervention, Cambridge, MA, USA, 11–13 October 1998; Springer: Berlin/Heidelberg, Germany; pp. 130–137.
58. Visvalingam, M.; Whyatt, J.D. The Douglas-Peucker Algorithm for Line Simplification: Re-evaluation through Visualization. In *Computer Graphics Forum*; Blackwell Publishing Ltd.: Oxford, UK, 1990; pp. 213–225.
59. Pingitore, N.; Clague, J.; Gorski, D. Round Top Mountain rhyolite (Texas, USA), a massive, unique Y-bearing-fluorite-hosted heavy rare earth element (HREE) deposit. *J. Rare Earths* **2014**, *32*, 90–96. [[CrossRef](#)]
60. Kopačková, V.; Chevrel, S.; Bourguignon, A.; Rojik, P. Application of high altitude and ground-based spectroradiometry to mapping hazardous low-pH material derived from the Sokolov open-pit mine. *J. Maps* **2012**, *8*, 220–230. [[CrossRef](#)]
61. Van der Meer, F.D.; Van der Werff, H.M.A.; Van Ruitenbeek, F.J.A.; Hecker, C.A.; Bakker, W.H.; Noomen, M.F.; Van der Meijde, M.; Carranza, E.J.M.; De Smeth, J.B.; Woldai, T. Multi- and hyperspectral geologic remote sensing: A review. *Int. J. Appl. Earth Obs. Geoinf.* **2012**, *14*, 112–128. [[CrossRef](#)]
62. Atzberger, C. Advances in remote sensing of agriculture: Context description, existing operational monitoring systems and major information needs. *Remote Sens.* **2013**, *5*, 949–981. [[CrossRef](#)]
63. Liaghat, S.; Balasundram, S.K. A review: The role of remote sensing in precision agriculture. *Am. J. Agric. Biol. Sci.* **2010**, *5*, 50–55. [[CrossRef](#)]
64. Foody, G.M. Remote sensing of tropical forest environments: Towards the monitoring of environmental resources for sustainable development. *Int. J. Remote Sens.* **2003**, *24*, 4035–4046. [[CrossRef](#)]
65. Shalaby, A.; Tateishi, R. Remote sensing and GIS for mapping and monitoring land cover and land-use changes in the Northwestern coastal zone of Egypt. *Appl. Geogr.* **2007**, *27*, 28–41. [[CrossRef](#)]
66. Mars, J.C.; Rowan, L.C. ASTER spectral analysis and lithologic mapping of the Khanneshin carbonatite volcano, Afghanistan. *Geosphere* **2011**, *7*, 276–289. [[CrossRef](#)]
67. Ninomiya, Y.; Fu, B. Thermal infrared multispectral remote sensing of lithology and mineralogy based on spectral properties of materials. *Ore Geol. Rev.* **2019**, *108*, 54–72. [[CrossRef](#)]
68. Rauhala, A.; Tuomela, A.; Davids, C.; Rossi, P.M. UAV remote sensing surveillance of a mine tailings impoundment in Sub-Arctic conditions. *Remote Sens.* **2017**, *9*, 1318. [[CrossRef](#)]
69. Tong, X.; Liu, X.; Chen, P.; Liu, S.; Luan, K.; Li, L.; Liu, S.; Liu, X.; Xie, H.; Jin, Y.; et al. Integration of UAV-based photogrammetry and terrestrial laser scanning for the three-dimensional mapping and monitoring of open-pit mine areas. *Remote Sens.* **2015**, *7*, 6635–6662. [[CrossRef](#)]
70. Lucieer, A.; De Jong, S.M.; Turner, D. Mapping landslide displacements using Structure from Motion (SfM) and image correlation of multi-temporal UAV photography. *Prog. Phys. Geogr.* **2014**, *38*, 97–116. [[CrossRef](#)]
71. Niethammer, U.; Rothmund, S.; James, M.R.; Travelletti, J.; Joswig, M. Nav-based remote sensing of landslides. *Int. Arch. Photogramm. Remote Sens. Spat. Inf. Sci.-ISPRS Arch.* **2010**, *38*, 496–501.
72. Bhardwaj, A.; Sam, L.; Martín-Torres, F.J.; Kumar, R. UAVs as remote sensing platform in glaciology: Present applications and future prospects. *Remote Sens. Environ.* **2016**, *175*, 196–204. [[CrossRef](#)]
73. Mancini, F.; Dubbini, M.; Gattelli, M.; Stecchi, F.; Fabbri, S.; Gabbianelli, G. Using unmanned aerial vehicles (UAV) for high-resolution reconstruction of topography: The structure from motion approach on coastal environments. *Remote Sens.* **2013**, *5*, 6880–6898. [[CrossRef](#)]
74. Rokhmana, C.A. The Potential of UAV-based Remote Sensing for Supporting Precision Agriculture in Indonesia. *Procedia Environ. Sci.* **2015**, *24*, 245–253. [[CrossRef](#)]
75. Aasen, H.; Honkavaara, E.; Lucieer, A.; Zarco-Tejada, P.J. Quantitative remote sensing at ultra-high resolution with UAV spectroscopy: A review of sensor technology, measurement procedures, and data correction workflows. *Remote Sens.* **2018**, *10*, 1091. [[CrossRef](#)]

76. Eltner, A.; Kaiser, A.; Castillo, C.; Rock, G.; Neugirg, F.; Abellan, A. Image-based surface reconstruction in geomorphometry—Merits, limits and developments of a promising tool for geoscientists. *Earth Surf. Dyn. Discuss.* **2015**, *3*, 1445–1508. [CrossRef]
77. Westoby, M.J.; Brasington, J.; Glasser, N.F.; Hambrey, M.J.; Reynolds, J.M. “Structure-from-Motion” photogrammetry: A low-cost, effective tool for geoscience applications. *Geomorphology* **2012**, *179*, 300–314. [CrossRef]
78. Carrivick, J.L.; Smith, M.W.; Quincey, D.J. *Structure from Motion in the Geoscience*; John Wiley & Sons: Hoboken, NJ, USA, 2016.
79. James, M.R.; Robson, S.; D’Oleire-Oltmanns, S.; Niethammer, U. Optimising UAV topographic surveys processed with structure-from-motion: Ground control quality, quantity and bundle adjustment. *Geomorphology* **2017**, *280*, 51–66. [CrossRef]
80. Senop. Optronics Hyperspectral. 2016. Available online: <http://www.rikola.fi/products/hyperspectral-camera/> (accessed on 8 November 2017).
81. Tommaselli, A.M.G.; Santos, L.D.; Berveglieri, A.; Oliveira, R.A.; Honkavaara, E. A study on the variations of inner orientation parameters of a hyperspectral frame camera. *Int. Arch. Photogramm. Remote Sens. Spat. Inf. Sci.* **2018**, *XLII-1*, 429–436. [CrossRef]



© 2019 by the authors. Licensee MDPI, Basel, Switzerland. This article is an open access article distributed under the terms and conditions of the Creative Commons Attribution (CC BY) license (<http://creativecommons.org/licenses/by/4.0/>).